REPUBLIC OF TÜRKİYE
YILDIZ TECHNICAL UNIVERSITY
GRADUATE SCHOOL OF SCIENCE AND ENGINEERING

DESIGN AND FABRICATION OF CONDUCTIVE POLYMER/ DOPED GRAPHENE OXIDE/SILICA COMPOSITE ANODES FOR LITHIUM-ION BATTERIES

Mohammed Mahdi Hussein ALBUJASIM

DOCTOR OF PHILOSOPHY THESIS

Department of of Metallurgical and Material Engineering

Program of Materials Science and Engineering

Supervisor

Prof. Dr.Metin GENÇTEN

April, 2026

REPUBLIC OF TÜRKİYE

YILDIZ TECHNICAL UNIVERSITY

GRADUATE SCHOOL OF SCIENCE AND ENGINEERING

DESIGN AND FABRICATION OF CONDUCTIVE POLYMER/ DOPED GRAPHENE OXIDE/SILICA COMPOSITE ANODES FOR LITHIUM-ION BATTERIES

A thesis submitted by Mohammed ALBUJASİM in partial fulfillment of the requirements for the degree of **DOCTOR OF PHILOSOPHY** is approved by the committee on 01.04.2026 in Department of Metallurgical and Material Engineering, Program of Materials Science and Engineering.

Prof. Dr. Metin GENÇTEN
Yildiz Technical University
Supervisor

Approved By the Examining Committee

Prof. Metin GENÇTEN, Supervisor
Yildiz Technical University _____

Prof. Nilgün KARATEPE YAVUZ, Member
Istanbul Technical University _____

Assoc. Prof. Buğra ÇİÇEK, Member
Yildiz Technical University _____

Assoc. Prof. Burak BİROL, Member
Yildiz Technical University _____

Assoc. Prof. Melih Beşir ARVAS, Member
Istanbul University _____

I hereby declare that the study entitled “Design and Fabrication of Conductive Polymer/ Doped Graphene Oxide/Silica Composite Anodes for Lithium-Ion Batteries” that I prepared under the supervision of Prof. Dr. Metin GENÇTEN was conducted in full compliance with the relevant legal requirements regarding data collection and data use; that all information obtained from other sources has been fully and properly acknowledged in the main text and references; that no fabrication and/or falsification has been made with respect to the research data or findings; and that throughout the study I have adhered to the principles of scientific research and academic ethics.

Generative Artificial Intelligence (GenAI) technologies were not employed at any stage of this thesis study, including its conceptualization, planning, execution, evaluation, or the writing process; the work was conducted entirely through my own original effort.

I accept full administrative and legal responsibility for any consequences that may arise if this declaration is determined to be false.

Mohammed Mahdi Hussein ALBUJASİM

Signature

This work was supported by Yildiz Technical University Scientific Research Council (BAP) under FCD-2022-5030 project code and FDK-2023-5814 Doctoral Project code.

Dedicated to my parents,

my wife,my son Ali,

and my daughter Zuha

ACKNOWLEDGEMENTS

First and foremost, I offer my deepest thanks to Allah, for granting me the strength and ability to complete this work. I would like to express my sincere appreciation to my supervisor, Prof. Dr. Metin GENÇTEN, for his invaluable guidance, continuous encouragement, and unwavering support throughout my doctoral studies. His mentorship extended well beyond academic supervision; his advice, motivation, and moral support—especially during challenging times—were crucial to the successful completion of this dissertation. He was not only an outstanding supervisor but also a genuine mentor and friend, treating me and every member of our research group with warmth and respect, like family.

I am also grateful to my colleagues and friends for fostering a collaborative, inspiring, and supportive academic environment. My sincere thanks go to the Gençten Research Group (GRG) and the YTU Waste Recycling Research Group (WRRG) at Yildiz Technical University for their technical assistance and academic contributions. I would like to extend my appreciation to our esteemed jury members, Prof. Dr. Nilgun Karatepe Yavuz and Assoc. Prof. Buğra ÇİÇEK, for their valuable comments, insightful suggestions, and constructive feedback. I am deeply thankful to my lab mates in the Gençten Research Group for their cooperation, encouragement, and friendship. You truly made the laboratory both a productive and enjoyable place for personal and professional growth. It has been a privilege to be part of this journey and to work alongside such an exceptional team. Finally, and most importantly, I express my heartfelt gratitude to my beloved family, my parents, my wife, my son Ali, and my daughters Zuha for their endless love, patience, and unwavering support. They have been my greatest source of strength and the reason I persevered. This achievement is not mine alone; it belongs to everyone who stood by me and supported me throughout this journey.

Mohammed Mahdi Hussein ALBUJASİM

TABLE OF CONTENTS

LIST OF ABBREVIATIONS ix
LIST OF FIGURES x
LIST OF TABLES xii
ABSTRACT xiii
ÖZET xv
1 INTRODUCTION 1
1.1 Introduction of Lithium Ion Battery……1
1.2 Operation Principle of Lithium Ion Battery……1
1.3 Materials for Anodes in Lithium-Ion Batteries……3
1.3.1 Graphitic and Carbonaceous Anode Materials……3
1.3.2 Conversion anode materials……4
1.3.3 Alloy based anode materials……4
1.4 Strategies To Overcome Challenges of Silicon Electrodes 6
1.4.1 Decrease in particle size……6
1.4.2 Composite Silicon Anodes for High-Performance Lithium-Ion Batteries……6
1.4.3 Amorphous Silicon vs Crystalline Silicon……10
1.5 Synthesis Methodes and Applications……11
2 EXPERIMENTAL 14
2.1 Chemicals……... 14
2.2 Preparation and characterization of heteroatom doped graphene…….. 14
2.3 Synthesis and characterization of polypyrrole…….. 15
2.4 Synthesis and characterization of polyaniline…… 16
2.5 Production and characterization of button cell type Li-ion batteries……. 17
2.6 Characterization Methods…… 20
3 RESULTS AND DISCUSSION 22
3.1 Characterazation of conducting polymer……... 22
3.1.1 Optimization of Polypyrrole synthesis……22
3.1.2 Optimization of Polyaniline synthesis……25

3.2 Characterization of doped graphene oxide…… 29
3.3 Electrochemical measurements…… 36
3.3.1 Reference samples (doped graphene oxide and fumed silica).....36
3.3.2 Polypyrrole samples 40
3.3.3 Polyaniline samples 48
4 CONCLUSION **58**
REFERENCES **60**
PUBLICATIONS FROM THE THESIS **68**

LIST OF SYMBOLS

$J\ mol^{-1}\ K^{-1}$	joules per mole per kelvin
$mAh\ g^{-1}$	milliampere-hour per gram
σ	Warburg coefficient.

LIST OF ABBREVIATIONS

Ag/AgCl	Silver/Silver Chloride
BET	Surface Area Measurements by Brunauer-Emmett-Teller
ClGO	Chlorine-doped graphene oxide powders
CV	Cyclic Voltammetry
EDS	Energy Dispersive X-ray Spectroscopy
EIS	Electrochemical Impedance Spectroscopy
F	Faraday constant (96485 C mol^{-1})
FT-IR	Fourier transform infrared spectrophotometry
GCD	Galvanostatic Charge and Discharge Tests
GO	Graphene oxide
Lα	Nanocrystalline domain size (nm)
LIBs	Lithium-ion batteries
NGO	Nitrogen Doped graphene oxide powder
Pt	Platinum
SEI	Solid-electrolyte interface
SEM	Scanning Electron Microscopy
SGO	Sulfur doped graphene oxide
XRD	X-Ray Diffractometer
Z’	Real resistance (ohm)
ZImg	Imaginary resistance (ohm)

LIST OF FIGURES

Figure 1.1 Schematic diagram of lithium-ion battery that employs graphitic carbon as anode and transition metal oxide LiMO2 as cathode [4]. **2**

Figure 2.1 Synthesis of doped graphene oxide with different doping elements. .. **15**

Figure 2.2 Synthesis of Polypyrrole. **16**

Figure 2.3 Synthesis of Polyaniline. **17**

Figure 2.4 A) Equivalent circuit model of one semi-circle and B) Equivalent circuit model of two semi-circles. **21**

Figure 3.1 A) Electrical conductivity of polypyrrol at different monomer concentration, B) SEM image of Pyrrol 0.1M, C) SEM image of Pyrrol 0.3M, and D) SEM image of Pyrrol 0.5M **23**

Figure 3.2 A) Electrical conductivity of polypyrrol at different acid concentration, B) FTIR of optimum polypyrrole C) SEM image of polypyrrole at 0.1M acid, C) SEM image of polypyrrole at 0.5M acid, and D) SEM image of polypyrrole 3M, and E) SEM image of polypyrrole 5M. **25**

Figure 3.3 A) Electrical conductivity of Pani at different monomer concentration, B) Electrical conductivity of Pani at different acid concentration, C SEM image of PANI 0.1, D) SEM images of PANI 0.3, E) SEM images of PANI 0.5, F SEM image of PANI S0.1, G) SEM images of PANI S0.5, H) SEM images of PANI S3, and I) FTIR spectrum of optimum polyaniline sample. **28**

Figure 3.4 Raman spectra of N-GO, S-GO, and Cl-GO. **30**

Figure 3.5 XPS spectra of N-GO, (A) O 1s, (B) C 1s and (C) N 1s. **32**

Figure 3.6 Common atomic configurations of nitrogen dopants in the graphene lattice. **32**

Figure 3.7 XPS survey spectra of the S-doped graphene; (A) C1s XPS spectra; (B) S 2p XPS spectra and (C) O1s**.** **33**

Figure 3.8 XPS survey spectra of the Cl-doped graphene; (A) C1s XPS spectra; (B) Cl2p XPS spectra; (C) O1s XPS spectra. **34**

Figure 3.9 Morphology of doped graphene oxide, (A) SEM of NGO, (B) TEM of NGO, (C) SEM of SGO, (D) TEM of SGO, (E) SEM of ClGO, and (F) TEM of ClGO. **35**

Figure 3.10 CV and charge-discharge at different rates, (A) CV of NGO, (B) Charge-discharge of NGO, (C) CV of SGO, (D) Charge-discharge of SGO, (E) CV of ClGO, and (F) Charge-discharge of ClGO. **38**

Figure 3.11 Cycling performance and EIS of doped graphene oxide, (A) Cycling performance of NGO, (B) EIS of NGO, (C) CV of SGO, (D) Cycling performance of SGO, (E) EIS of ClGO, and (F) Cycling performance of ClGO. **40**

Figure 3.12 Cycling voltammetry of samples, (A) N1-ppy, (B) N2-ppy, (C) S1-ppy, (D) S2-ppy, (E) Cl1-ppy, and (F) Cl2-ppy. **41**

Figure 3.13 Charge-discharge at different rates of samples, (A) N1-ppy, (B) N2-ppy, (C) S1-ppy, (D) S2-ppy, (E) Cl1-ppy, and (F) Cl2-ppy..... **43**

Figure 3.14 Comparasion of discharge capacity of polypyrrole samples. **44**

Figure 3.15 Cycling performance of ppy samples. **44**

Figure 3.16 EIS of samples, (A) N1-ppy, (B) N2-ppy, (C) S1-ppy, (D) S2-ppy, (E) Cl1-ppy, and (F) Cl2-ppy. **46**

Figure 3.17 Cycling voltammetry of samples, (A) N1-pani, (B) N2- pani, (C) S1-pani, (D) S2- pani, (E) Cl1- pani, and (F) Cl2- pani. **49**

Figure 3.18 charge-discgarge of samples, (A) N1-pani, (B) N2- pani, (C) S1- pani, (D) S2- pani, (E) Cl1- pani, and (F) Cl2- pani. **52**

Figure 3.19 Comparasion of discharge capacity for polyaniline samples. **54**

Figure 3.20 Cycling performance of pani samples. **54**

Figure 3.21 EIS of samples, (A) N1-pani, (B) N2- pani, (C) S1- pani, (D) S2- pani, (E) Cl1-pani, and (F) Cl2- pani. **56**

LIST OF TABLES

Table 2.1 All prepared batteries. **19**

Table 3.1 Surface areas of polypyrrole prepared with different concentration of pyrrole. **23**

Table 3.2 Surface areas of polypyrrole prepared with different concentration of sulfuric acid. **24**

Table 3.3 Surface area results of optimization synthesis for polyaniline. **27**

Table 3.4 Results of Raman analysis **30**

Table 3.5 Surface area of doped graphene oxide **35**

Table 3.6 Resistancs values form EIS before and after cycling of polypyrrole samples. **47**

Table 3.7 Resistancs values form EIS before and after cycling of polyaniline samples. **57**

ABSTRACT

DESIGN AND FABRICATION OF CONDUCTIVE POLYMER/ DOPED GRAPHENE OXIDE/SILICA COMPOSITE ANODES FOR LITHIUM-ION BATTERIES

Mohammed Mahdi Hussein ALBUJASIM

Department of Metallurgical and Material Engineering

Doctor of Philosophy Thesis

Supervisor: Prof. Dr. Metin GENÇTEN

Lithium-ion batteries (LIBs) are among the most promising energy storage systems for portable electronics and electric vehicles due to their high energy density, long cycle life, and environmental compatibility. However, the limited theoretical capacity of commercial graphite anodes (372 mAh g^{-1}) restricts further improvements in battery performance. In this study, new-generation composite anode materials based on heteroatom-doped graphene oxide (N-, S-, and Cl-doped GO), conductive polymers (polypyrrole (PPy) and polyaniline (PANI)), and fumed silica were synthesized and systematically investigated to enhance electrochemical performance. Heteroatom-doped graphene oxide powders were produced via a one-step electrochemical method under acidic media using chronoamperometry. Conductive polymers were synthesized through chemical oxidative polymerization, and their synthesis parameters were optimized in terms of monomer and acid concentration to achieve maximum electrical conductivity and surface area. The prepared materials were characterized by XRD, SEM-EDX, FT-IR, Raman spectroscopy, BET surface area analysis, TGA, and four-point probe conductivity measurements.

Composite anodes were fabricated by combining doped graphene oxide, conductive polymers, and silica in various compositions and assembled into CR2032-type coin cells using lithium metal as the counter electrode. Electrochemical performances were evaluated by cyclic voltammetry (0.02–3 V), galvanostatic charge–discharge tests at different C-rates (0.1C–10C), and long-term cycling (100 cycles at 10C). The results demonstrated that the incorporation of conductive polymers significantly improved electrical conductivity and structural stability, while heteroatom doping enhanced active sites and lithium-ion diffusion kinetics. conductive polymers acted as a buffering matrix, mitigating volume changes of silica during cycling. Among all compositions, low ratio of N-doped graphene/PPy give good cycling performance at high rate but low capacity at low rate and high ratio N-doped graphene/PANI composites exhibited superior specific capacity, improved rate capability, and enhanced cycling stability compared to undoped and single-component systems.

This study provides a scalable and cost-effective strategy for designing high-performance composite anodes and contributes to the development of next-generation lithium-ion batteries with improved capacity and durability.

Keywords: Lithium-ion battery, heteroatom-doped graphene oxide, polypyrrole, polyaniline, silica.

ÖZET

LİTYUM-İYON PİLLER İÇİN İLETKEN POLİMER/KATKILANMIŞ GRAFEN OKSİT/SİLİKA KOMPOZİT ANOTLARIN TASARIMI VE ÜRETİMİ

Mohammed Mahdi Hussein ALBUJASIM

Metalurji ve Malzeme Mühendisliği Anabilim Dalı

Doktora Tezi

Danışman: Prof. Dr. Metin GENÇTEN

Lityum-iyon piller (LIB'ler), yüksek enerji yoğunluğu, uzun çevrim ömrü ve çevre dostu özellikleri sayesinde taşınabilir elektronik cihazlar ve elektrikli araçlar için en umut verici enerji depolama sistemleri arasında yer almaktadır. Ancak ticari grafit anotların sınırlı teorik kapasitesi (372 mAh g^{-1}), pil performansının daha fazla geliştirilmesini kısıtlamaktadır. Bu çalışmada, elektro-kimyasal performansı artırmak amacıyla heteroatom katkılı grafen oksit (N-, S- ve Cl katkılı GO), iletken polimerler (polipirol (PPy) ve polianilin (PANI)) ve füme silika esaslı yeni nesil kompozit anot malzemeleri sentezlenmiş ve sistematik olarak incelenmiştir. Heteroatom katkılı grafen oksit tozları, asidik ortamda kronoamperometri kullanılarak tek adımlı elektrokimyasal yöntem ile üretilmiştir. İletken polimerler kimyasal oksidatif polimerizasyon yöntemi ile sentezlenmiş ve maksimum elektriksel iletkenlik ile yüzey alanı elde etmek amacıyla monomer ve asit konsantrasyonları optimize edilmiştir. Hazırlanan malzemeler XRD, SEM-EDX, FT-IR, Raman spektroskopisi, BET yüzey alanı analizi, TGA, elementel analiz ve dört nokta prob iletkenlik ölçümleri ile karakterize edilmiştir.

Kompozit anotlar, farklı oranlarda katkılı grafen oksit, iletken polimer ve silikanın birleştirilmesiyle hazırlanmış ve karşı elektrot olarak lityum metal kullanılarak CR2032 tipi düğme piller hâlinde monte edilmiştir. Elektrokimyasal performanslar 0.02–3 V aralığında döngüsel voltametri, farklı C oranlarında (0.1C–10C) galvanostatik şarj–deşarj testleri ve 10C'de 100 çevrimlik uzun dönem çevrim testleri ile değerlendirilmiştir.

Elde edilen sonuçlar, iletken polimer ilavesinin elektriksel iletkenliği ve yapısal kararlılığı önemli ölçüde artırdığını; heteroatom katkısının ise aktif merkez sayısını ve lityum-iyon difüzyon kinetiğini geliştirdiğini göstermiştir. Silika, çevrim sırasında oluşan hacim değişimlerini azaltan tampon bir matris görevi görmüştür. Tüm kompozisyonlar arasında, optimize edilmiş N-katkılı grafen/PPy ve N-katkılı grafen/PANI kompozitleri, katkısız ve tek bileşenli sistemlere kıyasla daha yüksek özgül kapasite, gelişmiş hız performansı ve üstün çevrim kararlılığı sergilemiştir.

Bu çalışma, yüksek performanslı kompozit anotların tasarımı için ölçeklenebilir ve maliyet etkin bir strateji sunmakta ve artırılmış kapasite ile dayanıklılığa sahip yeni nesil lityum-iyon pillerin geliştirilmesine katkı sağlamaktadır.

Anahtar Kelimeler: Lityum-iyon pil, heteroatom katkılı grafen oksit, polipirol, polianilin, silika.

1
INTRODUCTION

1.1 Introduction of Lithium Ion Battery

A battery is a portable electrochemical device that converts stored chemical energy into electrical energy. Its unique function has made it extremely popular in our daily lives. It is a popular power source for both residential and industrial uses. Since Alessandro Volta devised the Voltaic Pile in 1800, battery technology has advanced rapidly. Nowadays, there are two basic types of batteries: primary batteries and secondary batteries. Secondary batteries are rechargeable due to their reversible electrochemical processes. Many efforts have been made over the last century to create secondary batteries [1]. Lithium-ion batteries are among the most common types of secondary batteries because of their high energy density, strong cycle performance, and lack of memory effect. They are frequently used to power a variety of portable devices including mobile phones, camcorders, and laptop computers. Recently, scientists in the departments of chemistry, chemical engineering, and materials science have focused on increasing the energy density of lithium-ion batteries for use in electric vehicles (EV) [2][3]. Due to the energy crisis and environmental concerns, the development of EV is required. Lithium-ion batteries are among the most promising rechargeable batteries for electric vehicles.

1.2 Operation Principle of Lithium Ion Battery

A lithium-ion battery is typically composed of four parts: cathode, anode, separator and electrolyte. Two electrodes (cathode and anode) act as lithium ions insertion hosts. Lithium ions are shuttled between them. Different lithium-ion insertion materials have different electrochemical potentials. A separator is placed between the two electrodes to prevent short circuits. The electrolyte is usually a mixture of organic carbonates with Li-containing salts. The electrolyte is electrically inert but allows lithium ions migrate through during

charging/discharging. Take lithium-ion battery with LiMO2 as cathode, graphitic carbon as anode, for example, the basic principle of lithium-ion battery can be illustrated by Figure 1.1. During a discharge process, lithium ions are released from the anode and migrate to the cathode through electrolyte. Meanwhile, electrons are also released from anode and move to cathode through the external circuit to maintain the charge conservation. When all the lithium ions from anode have migrated to the cathode, the anode materials totally change from LiC6 to C and the cathode materials change from MO2 to LixMO2. It is obvious that the chemical valences of both C and M elements have changed after discharge. Thus, redox reaction has taken place. During a charging process, lithium ions and electrons move in the opposite direction. Reverse redox reaction takes place at anode and cathode. Oxidation and reduction reactions occur at anode and cathode are as follows with discharging being forwards:

$$LixCn \leftrightarrow nC + xLi+ + xe- \quad (1.1)$$

$$Li1\text{-}xMO2 + xLi+ + xe- \leftrightarrow LiMO2 \quad (1.2)$$

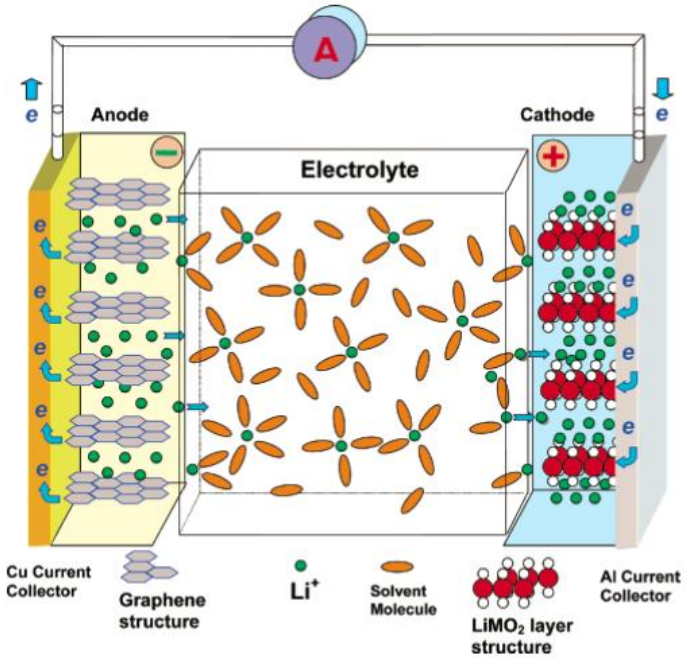


Figure 1.1 Schematic diagram of lithium-ion battery that employs graphitic carbon as anode and transition metal oxide LiMO2 as cathode [4].

1.3 Materials for Anodes in Lithium-Ion Batteries

Lithium metal was initially employed as the anode material in rechargeable lithium batteries due to its exceptionally high theoretical capacity and low electrochemical potential. However, during repeated charge–discharge cycles, lithium deposition on the anode surface frequently leads to the formation of dendritic structures. These dendrites can penetrate the separator, causing short internal circuits, poor cycling stability, and significant safety hazards. Consequently, alternative anode materials have been developed for lithium-ion batteries (LIBs) to ensure improved safety and long-term performance.

1.3.1 Graphitic and Carbonaceous Anode Materials

Currently, graphitic carbon represents the most widely employed commercial anode material in lithium-ion batteries (LIBs). It can be obtained from a variety of carbon precursors, including natural graphite as well as synthetic sources such as polymer resins. Variations in synthesis and post-treatment methods produce carbon materials with diverse structural and electrochemical characteristics. Carbon-based anodes are generally categorized into three main types: graphite, hard carbon, and soft carbon. Graphite, in particular, exhibits a well-ordered layered structure composed of ABAB-stacked graphene sheets held together by van der Waals forces. During battery operation, lithium ions reversibly intercalate between these graphene layers, forming the compound LiC_6, which corresponds to a theoretical specific capacity of 372 mAh g^{-1}.The lithium intercalation mechanism and electrochemical behavior of graphite have been extensively investigated. [18]. Carbon remains an attractive anode material due to its natural abundance, relatively low cost, and minimal volume change during lithiation and delithiation. To further enhance its electrochemical performance, various strategies such as particle coating, surface modification, and nanostructuring have been widely explored to improve cycling stability and rate capability. Despite these advancements, carbon-based anodes still exhibit certain limitations, including irreversible capacity loss during the first cycle and restricted long-term cycling performance. Moreover, their relatively low theoretical specific capacity limits their application in high-energy-density and large-scale energy

storage systems. Therefore, the primary challenge in developing next-generation carbon-based anodes lies in increasing specific capacity while maintaining excellent cycling stability.

1.3.2 Conversion anode materials

Transition metal compounds with the general formula M_xN_y(where M =Fe, Co, Cu, Mn, Ni and N =O, P, S, or N) and their corresponding lithium-containing products exhibit high reversible capacities in the range of 500–1000 mAh/g. This enhanced capacity arises from the involvement of multiple electrons in electrochemical conversion reactions [5]. Because of their low cost and environmentally acceptable properties, iron oxides have been intensively researched as conversion materials for LIB. However, iron oxides have poor cycling performance because of low electrical conductivity, low Li-ion diffusion, excessive volume expansion, and iron agglomeration during charging and discharging. Several attempts have been taken to alleviate these disadvantages, including changing size, shape, and porosity [6]. For instance, Y. Zhu et al [7]. used interconnected porous α-Fe2O3 nanorods as anode material. The interconnected porous α-Fe2O3 nanorods are produced using a simple hydrothermal calcination process. The α-Fe2O3 nanorods have a high initial discharge capacity of 740.2 mAh g-1 and maintain outstanding cycle stability at high-rate density (600 mAh g-1 at 0.5C and 520 mAh g-1 at 1C) after 300 cycles. The increased electrochemical characteristics can be due to the uniform 1D nanostructure, the interconnected nanostructure, and the large number of voids in the nanorod.

1.3.3 Alloy based anode materials

A variety of metals are capable of reacting with significant amounts of lithium, making them attractive candidates for anode materials in lithium-ion batteries (LIBs). Notable examples include Si, Sn, Mg, Bi, In, Zn, Ag, Au, Cd, Ga, and Ge. Nevertheless, the high cost of many of these metals has limited extensive research and practical application to only a select few. However, due to the high cost of some of these elements, only a limited number have been extensively investigated for practical applications. Alloy-based anodes generally exhibit very high theoretical specific capacities compared to conventional graphite. This high capacity originates from the multiple-electron alloying reactions between lithium

and the host metal. Nevertheless, a major challenge associated with these materials is the severe volume expansion that occurs during lithiation. The repeated alloying and de-alloying processes induce significant mechanical stress, leading to particle pulverization, electrode cracking, loss of electrical contact, and ultimately rapid capacity fading. To mitigate the detrimental effects of volume fluctuations, nanostructuring strategies have been widely employed. Reducing the active material to the nanoscale can effectively accommodate strain and improve structural stability, resulting in enhanced cycling performance [8]. Beyond particle size reduction, several additional strategies have been proposed to suppress volume change: 1) Embedding Li-alloys within mechanically flexible, lithium-ion-conductive metals or polymer matrices. 2) Embedding alloy particles within a matrix capable of buffering or partially constraining the volume expansion [9]. One particularly effective approach involves dispersing alloy particles within a conductive polymer matrix. In this configuration, the conductive polymer forms continuous electron-transport pathways between alloy particles, thereby enhancing electrical conductivity. Moreover, the intrinsic flexibility of the polymer matrix accommodates the substantial volume variations that occur during repeated alloying and de-alloying cycles [10]. For example, Jie Cai [11] integrated silicon nanoparticles into a conductive polyaniline template. The resulting composite exhibited significantly improved cycling stability and rate capability compared with pure nano-silicon. Among alloy-type anode materials, silicon has attracted considerable attention due to its exceptionally high theoretical capacity of approximately 4200 mAh/g, corresponding to full lithiation to $Li_{22}Si_5$, as well as its natural abundance and relatively low cost [12]. These attributes make silicon one of the most promising candidates for next-generation high-energy-density LIBs. [12]. Si may alloy with lithium to generate a variety of alloys, including Li12Si7, Li14Si6, Li13Si4, Li15Si4, Li22Si5, and others. The alloying process for the richest lithium phase is as follows: 22Li+ + 5Si + 22e- ↔ Li22Si5 [13]. The effective use of silicon anodes in Lithium-Ion Batteries might result in a more than ten times improvement in anode specific capacity when compared to industrial systems available now. When combined with a typical cathode and electrolyte, the overall capacity can be doubled. However, the large volume fluctuations (up to 400%) that occur throughout the lithiation/de-lithiation reactions continue to limit the application of this technology [14].

1.4 Strategies To Overcome Challenges of Silicon Electrodes

1.4.1 Decrease in particle size

Reducing the size of particles has been shown to be an efficient method of reducing stress inside the Si electrode. When compared to typical Si, nanosized Si exhibits less distortion and greater resistance to fracture due to volume expansion. Reducing the active elements has been shown to improve Li ion propagation kinetics, the stability of the initially created SEI layer, and the electrodes' fracture durability. The primary advantage of smaller particle sizes is their ability to efficiently alleviate mechanical stress caused by severe volume variations. This has resulted in extensive research on various types of nanostructures such as nanoparticles, nanowires[15], nanotubes[16][17], nanocomposites [18][19], and nanofilms [20][21][22] in recent years, with the objective of overcoming the disadvantages of bulk Si material and optimizing performance for practical application.

1.4.2 Composite Silicon Anodes for High-Performance Lithium-Ion Batteries

Silicon composite anodes are commonly fabricated by incorporating silicon into carbon-based materials, metallic elements, or elastic polymer matrices. These composite designs are intended to overcome the major limitations of pure silicon, namely severe volume expansion during lithiation and limited electrical conductivity.

1.4.2.1 Silicon/Carbon Composite Anodes

The incorporation of carbon materials or carbon coatings into silicon-based anodes is an effective strategy to establish continuous electrical pathways between silicon particles and the overall electrode structure. This approach not only enhances electrical conductivity but also improves structural stability during cycling. A wide range of synthesis strategies have been explored for the preparation of Si/C composites. These approaches include mechanical alloying of silicon with various carbon precursors through high-energy ball milling, deposition of silicon dioxide onto carbon frameworks followed by chemical reduction, chemical or thermal vapor deposition techniques, and thermal decomposition of silicon–carbon-containing precursors. For instance, Guo et al. [23] fabricated a Si/C composite by

mechanically milling silicon with polypyrrole and subsequently converting the polymer into carbon through pyrolysis. The final material, which contained roughly 10 wt.% silicon, demonstrated a stable reversible capacity of approximately 1000 mAh/g. In a related study, Zhang et al. [24] produced a Si/C composite with a lamellar microstructure by ball milling silicon particles together with carbon nanotubes. The composite delivered an initial specific capacity close to 1500 mAh/g and maintained a reversible capacity of 584 mAh g^{-1} after 20 charge–discharge cycles. Lanyao Shen et al. [25] adopted a different strategy by synthesizing a three-dimensional porous silicon structure via the magnesiothermic reduction of diatomaceous earth. Following acid treatment with HCl, the resulting material exhibited a highly porous architecture with an average pore size of approximately 200 nm, closely preserving the morphology of the original diatomite. This porous silicon anode showed an initial discharge capacity of 1818 mAh/g and retained 633 mAh/g after 30 cycles. Beyond conventional carbon matrices, graphene has attracted significant attention as a component in silicon-based composites Owing to its two-dimensional structure, exceptional electrical conductivity, large surface area, and robust mechanical and thermal properties, graphene serves as an effective conductive and structural support for silicon nanoparticles. Graphene/nanosilicon composites have been widely reported to enhance cycling durability. For example, composites constructed from graphene sheets obtained through thermal expansion of graphite exhibited excellent electrochemical behavior, achieving an initial capacity of 2750 mAh/g with approximately 83% capacity retention after 30 cycles. In addition, Zhou et al. [26] introduced nanosilicon into graphene sheets via a combined freeze-drying and thermal reduction process. Compared with pristine nanosilicon, the resulting Si/graphene composite demonstrated markedly improved cycling stability as well as enhanced rate performance.

1.4.2.2 Silicon-Based Composites with Active Host Matrices

In this category of anode materials, both silicon and the supporting matrix participate in the electrochemical reaction with lithium, forming lithium-based alloys during cycling. The fundamental concept is that while one component actively alloys with lithium, the second component functions as a buffering phase to accommodate the significant volume variations associated with lithiation and

delithiation, owing to the difference in their alloying potentials. Representative examples of such systems include SiSn and Mg_2Si-based composites. Xiao et al. [27] developed a distinctive nanostructured Si–Sn thin film through phase separation, which effectively suppressed mechanical deterioration by inhibiting the initiation and propagation of microcracks during repeated charge–discharge cycles. In particular, the optimized $Si_{54}Sn_{46}$ composition, composed of amorphous silicon nanoparticles homogeneously dispersed within a tin matrix, demonstrated remarkable cycling stability. This composite brought a high specific capacity of approximately 1420 mAh/g at 25 cycles. The enhanced electrochemical performance was attributed to the buffering role of the Sn matrix, which accommodated volume changes and suppressed microcrack formation during repeated lithiation and delithiation processes. Similarly, J. M. Yan et al. [28] Mg_2Si/C composites were fabricated through mechanically activated annealing of Mg and Si, followed by ball milling with CNTs and CMS at different composition ratios.. The optimized composite exhibited a reversible capacity of approximately 400 mAh/g with satisfactory cycling stability. The improved electrochemical behavior of these composites was primarily attributed to reduced charge-transfer resistance, the formation of a stable electrode–electrolyte interphase, and effective mitigation of volume expansion during cycling. These results highlight the importance of structural engineering and conductive matrix incorporation in enhancing the durability and performance of alloy-based anode materials.

1.4.2.3 Silicon-Based Composites with Inert Structural Matrices

In this type of silicon composite anode, silicon particles are uniformly embedded within an electrochemically inert matrix engineered to buffer the substantial volumetric changes occurring during lithiation. Such inactive frameworks commonly incorporate metallic elements including Fe, Co, Ni, and Ca.[29], metal oxides including Al_2O_3 [30] and Li_2O [31], as well as ceramic phases such as Si_3N_4 [32], and SiC. Although these matrices enhance structural stability, their incorporation often results in a reduction of reversible capacity due to their electrochemical inactivity.Heon-Young Lee et al. [33] developed a carbon-coated nano-silicon dispersed oxide/graphite composite through the mechanochemical reduction of SiO using aluminum, followed by ball milling and pyrolysis of coal–

tar pitch under an argon atmosphere. The resulting composite showed good cycling stability and a relatively low first-cycle irreversible capacity. These improvements were attributed to the uniform dispersion of nanoscale silicon, enhanced electronic and ionic conductivity provided by the carbon coating, and the buffering effect of the graphite matrix. Similarly, Liu et al. [31] The reported silicon composite consisted of nanosized Si particles uniformly embedded within a porous and mechanically resilient oxide/carbon conductive network. It was synthesized through the mechanochemical reduction of SiO, followed by pyrolysis of poly (vinyl chloride–covinyl acetate) to form the carbonaceous framework. Electrochemical testing demonstrated a sustained reversible capacity of around 625 mAh/g for 100 cycles, indicating excellent structural stability during cycling. However, a major drawback of incorporating inactive components is the potential hindrance of lithium-ion diffusion and electron transport toward the silicon phase, which can ultimately limit the achievable capacity. Therefore, the selection of inactive matrices should satisfy two key criteria: (i) high ionic and electronic conductivity, and (ii) sufficient mechanical robustness to withstand repeated volume fluctuations. Carbon coatings, owing to their high electronic conductivity, are particularly effective in buffering silicon's large volume changes and ensuring uniform dispersion of Si particles, thereby preventing agglomeration. Alternatively, conductive polymer matrices such as polypyrrole (PPy) or polyaniline (PANI) can serve as flexible and conductive hosts for silicon. These polymers exhibit electrochemical stability within the potential range of 0.0–2.0 V vs. Li/Li^+ and possess sufficient mechanical flexibility to withstand volume expansion and contraction during repeated cycling. As a result, they contribute to improved cycling stability and enhanced rate performance. A Si/PEDOT:PSS composite was fabricated by polymerizing EDOT in situ in the presence of nanoscale silicon dispersed within an aqueous PSS medium [34] Electrochemical evaluation revealed an initial discharge capacity of 1096 mAh/g and a first-cycle coulombic efficiency of 85%. Despite a gradual capacity reduction from 664 mAh/g after 20 cycles to 257 mAh/g after 50 cycles, the composite demonstrated significantly improved structural and electrochemical stability relative to bare silicon anodes. Similarly, Jian Cai et al. [11] A nano-Si/PANI composite was developed with silicon nanoparticles homogeneously dispersed within a nest-like polyaniline structure. The enhanced electrochemical performance, including superior cycling durability

and increased reversible capacity, was primarily associated with improved silicon dispersion and efficient electron transport enabled by the conductive polymer matrix. Furthermore, S.Y. Chew et al. [35] synthesized a n-silicon/polypyrrole compound through the in-situ polymerization of pyrrole, forming a conductive polymer coating around the silicon particles to enhance structural integrity and electrochemical performance. Compared with pure silicon anodes, the Si/PPy electrodes exhibited significantly enhanced cycling stability, as the PPy matrix formed a conductive network capable of buffering silicon's substantial volume variations and preventing electrode cracking and pulverization during repeated lithiation/delithiation processes.

1.4.3 Amorphous Silicon vs Crystalline Silicon

Both crystalline silicon (c-Si) and amorphous silicon (a-Si) are electrochemically active toward lithium; however, their lithiation and delithiation mechanisms differ significantly. Crystalline silicon undergoes lithiation through a two-phase reaction pathway, in which c-Si is progressively transformed into amorphous lithiated silicon (a-Li_xSi). In situ transmission electron microscopy (TEM) observations have demonstrated the presence of a distinct reaction interface, approximately 1 nm in thickness, separating the lithiated region from the remaining crystalline silicon [36]. This two-phase behavior is primarily attributed to the high activation energy required to disrupt the strong covalent Si–Si bonds within the crystalline lattice [37]. Moreover, lithiation of c-Si exhibits pronounced anisotropy, with lithium preferentially inserting along the ⟨110⟩ crystallographic direction. This directional dependence has been associated with the lower lithium diffusion energy barrier at the Si–electrolyte interface along the ⟨110⟩ orientation [38]. During the initial lithiation cycle, crystalline silicon experiences a solid-state amorphization process and subsequently remains in an amorphous state in the following cycles [39][40]. In contrast, amorphous silicon demonstrates isotropic lithiation behavior due to the absence of long-range crystalline order. Nevertheless, despite its structural uniformity, the detailed lithiation mechanism of amorphous silicon remains a subject of ongoing scientific debate.

1.5 Synthesis Methodes and Applications

Graphene is an important carbon-based material that was discovered in 2004 and has attracted great interest among researchers due to its many superior physical, chemical, electrical and optical properties [41]. For this reason, graphene-based materials have found important applications in many different fields, especially in energy storage systems. Especially heteroatom doped graphene oxides doped with heteroatoms (chlorine, Cl; nitrogen, N; sulfur, S) and containing oxygen in their structure have been used in important energy storage systems such as supercapacitors, Li-ion batteries and redox fluid batteries thanks to their conductivity properties and chemical activity [42]. Methods such as chemical method (Hummers method), chemical vapor deposition method and electrochemical deposition method are widely used in the production of hetero atom doped graphene oxide materials [43]. However, these methods have significant disadvantages in themselves. In the Hummers method, known as the chemical method, the production process involves approximately thirteen steps including oxidation/reduction, filtration, purification, drying, doping, etc. [44]. In addition, the method has significant disadvantages both in terms of the environmental hazards of the expensive oxidizing/reducing agents used and the high temperature applied in process. Again, the structures in the hetero atom doped graphene sheets produced cannot be controlled by this method. Chemical vapor deposition method, on the other hand, involves approximately seven steps and has significant disadvantages such as temperature/pressure effects applied during production [45]. At this point, electrochemical methods offer a significant advantage in graphene production with their environmentally friendly, low-cost and one-step production methods. In the electrochemical precipitation method, which is widely used in the literature, graphene is produced in expensive ionic liquids by reaching very high potential values (>8 V) [46]. Especially the high voltage values applied increase the cost in terms of energy and ionic liquids increase the cost in terms of consumables. At this point, the heteroatom doped graphene production method, which is carried out in acidic medium in a single step and at room conditions using the alternating voltammetry and chronoamperometric method known as Yücel method, offers an economic advantage in the production of graphene powders for use in many different fields [47][48]. Many studies using graphene in Li-ion batteries are

available in the literature. Graphene-based materials can be covalently doped with heteroatoms such as nitrogen, sulfur and chlorine, thereby significantly improving the performance of Li-ion batteries with the defect points created in the graphene structure. However, the low specific capacity of the reaction between carbon and Li+ ion decreases the performance of Li-ion batteries. In addition, the low porosity surface of heteroatom-doped graphene-based materials decreases the reversibility of the discharge reaction for Li-ion batteries, which reduces the maximum number of cycles that the battery can reach. At this point, the creation of composites of graphene-based materials with high porosity and high specific capacity to react with Li+ ion will play a critical role in improving battery performance.

Conductive polymers are lighter, cheaper and can show superior electrical conductivity when doped, like other conductive materials. In addition, their internal resistance is lower than graphene and carbon-based materials. Because of its porous structure, it provides high surface area interaction as an electrode material. Due to their superior properties such as high electrical conductivity, high coulombic efficiency and low degradation rates, the use of these materials as anode materials in Li-ion batteries has become an important issue [49]. In addition, the type of conductive polymer significantly affects the specific capacity of Li-ion batteries. Polypyrrole and polyaniline has been synthesized by many methods, including ultrasonication[50][51], Vapor phase polymerization (VPP)[52][53][54], electrochemical polymerization[55][56], Electrospinning[57], Microemulsion polymerization[58], photochemical preparation[59].This methods has some disadvantages such as in ultrasonication CPs can be damaged if the ultrasonication is too aggressive and/or too long, VPP method has Poor adhesion of CPs molecules to the substrate surface, electrochemical polymerization has drawbacks such as (High oxidation potential could lead to overoxidation of the polymer, Some monomers are theoretically unable to electropolymerize and Costly and time consuming method).In Electrospinning can be synthesis only soluble and thermoplastic polymers are applicable, Microemulsion polymerization require large amount of surfactant or co- surfactant to produce effective stabilization, and photochemical preparation the illumination is required and not all CPs can be produced via this method. The chemical polymerization[60] is used more frequently due to the simpler operation, providing diverse available methods to synthesize

different Conducting polymers (CPs), efficient to produce bulk quantities in the form of dispersion, powder and coating and permitting the large-scale production of these materials, which is currently impossible with electrochemical synthesis[61][62]. Although conductive polymers have high specific capacity for Li-ion batteries as anode material, their low mechanical stability is an important problem affecting battery performance. For this reason, it is important to create composites for the conductive polymer structures to be used in Li-ion batteries in a way that will eliminate this deficiency.

2
EXPERIMENTAL

2.1 Chemicals

Nitric acid, perchloric acid, and sulfuric acid were obtained from Merck and used as the reaction and doping medium. A graphite rod (Ø6X200E, 99.9%, 0.5 cm diameter) served as the working electrode and carbon source. Sigma-Aldrich provided pyrrole, and Aniline.

2.2 Preparation and characterization of heteroatom doped graphene

The -S, -N, and -Cl doped graphene oxide-based materials will be produced using the electrochemical method. The powder materials will be prepared in a 3-electrode electrochemical system using a graphite rod. In this method, a graphite rod will be used as the working electrode, platinum wire as the counter electrode, and silver / silver chloride (in 3 M potassium chloride) as the reference electrode. The chronoamperometry method will be employed in the preparation of graphene oxide powders, and a constant voltage of 2.3 V will be applied in the production of powders. The production of N-doped graphene oxide (N-GO) powders will be accomplished using a 5 M nitric acid solution. In contrast, S-doped graphene oxide (S-GO) powders will be synthesized via a 5 M sulfuric acid medium. Finally, Cl-doped graphene oxide (Cl-GO) powders will be fabricated using a 5 M perchloric acid solution as shown in Figure 2.1. The powders to be obtained will undergo a series of procedures, including filtration, washing, drying, grinding, and characterization via a range of analytical methods, including SEM, SEM-EDX, XPS, BET analysis, and Raman spectroscopy. These characterization studies will provide valuable insights into the composition and properties of the powders. Subsequently, the powders will be utilized in the production of active material for Li-ion batteries.

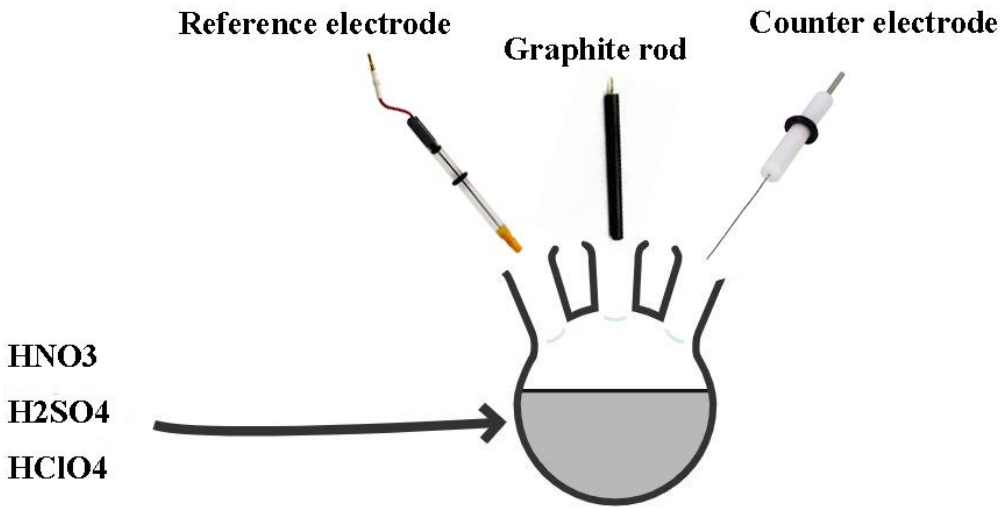


Figure 2.1 Synthesis of doped graphene oxide with different doping elements.

2.3 Synthesis and characterization of polypyrrole

In the synthesis of polypyrrole (PPy), which will be used as a conductive polymer, FeCl3 will be added into the sulfuric acid solution as an oxidant and then monomer (pyrrole) will be added to the system to produce the material. In the conductive polymer to be produced, the acid concentration and monomer concentration used in the production will be optimized. First, 1 M H2SO4 will be kept constant, and the monomer pyrrole will be added to the system at concentrations of 0.1 M, 0.3 M and 0.5 M respectively and PPy synthesis will be realized as shown in Figure 2.2. The surface areas and pore structure of the washed and dried conducting polymers will be determined by BET analysis. The mixture with the highest surface area will be considered as the optimum pyrrole concentration value. Then, keeping the optimum pyrrole concentration constant, the synthesis process will be repeated with H2SO4 concentrations of 0.1 M, 0.5 M, 1 M, 3 M and 5 M, respectively. The resulting mixtures will be subjected to BET analysis again and the acid concentration with the highest surface area and pore structure will be considered as the most suitable H2SO4 concentration. During these processes, the oxidant concentration (0.1 M) will be kept constant, and all reactions will be carried out at 70 ºC. Following three washes of the produced PPy's

with distilled water and ethyl alcohol, characterization procedures will be carried out by SEM, FT-IR, and EDX.

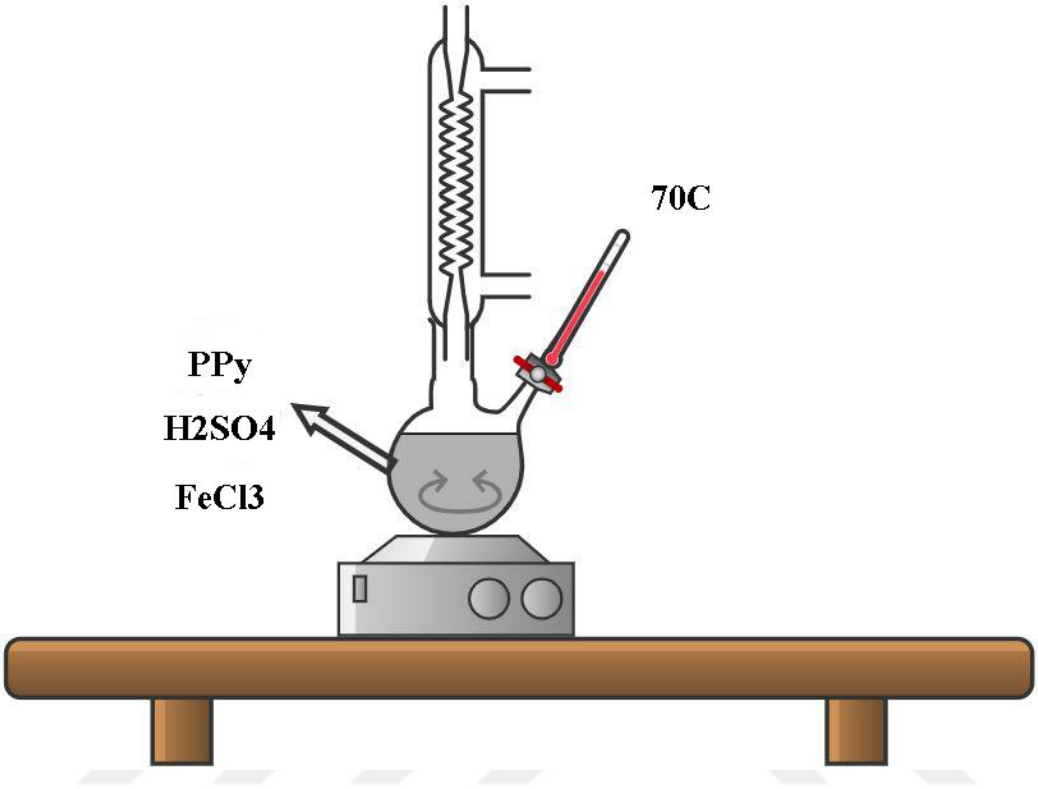


Figure 2.2 Synthesis of Polypyrrole.

2.4 Synthesis and characterization of polyaniline

In the synthesis of polyaniline (PANI), which will be used as a conductive polymer, oxidant (FeCl3) will be added into the sulfuric acid solution and then monomer (aniline) will be added to the system to produce the material. In the conductive polymer to be produced, the acid concentration and monomer concentration used in the production will be optimized. First, 1 M H2SO4 will be kept constant and PANI synthesis will be realized by adding the monomer aniline to the system at concentrations of 0.1 M, 0.3 M and 0.5 M respectively as shown in Figure 2.3. The surface areas and pore structure of the washed and dried conducting polymers will be determined by BET analysis. The mixture with the highest surface area will be considered as the optimum aniline concentration value. Then, keeping the optimum aniline concentration constant, the synthesis process will be repeated with H2SO4 concentrations of 0.1 M, 0.5 M, 1 M, 3 M and 5 M, respectively. The

resulting mixtures will be subjected to BET analysis again and the acid concentration with the highest surface area and pore structure will be considered as the most suitable H2SO4 concentration. During these processes, the oxidant concentration (0.1 M) will be kept constant, and all reactions will be carried out at 70 ºC. Characterization of the produced PANIs will be carried out by SEM, FT-IR, EDX, BET and TG-DTA analyses following three washes with distilled water and ethyl alcohol.

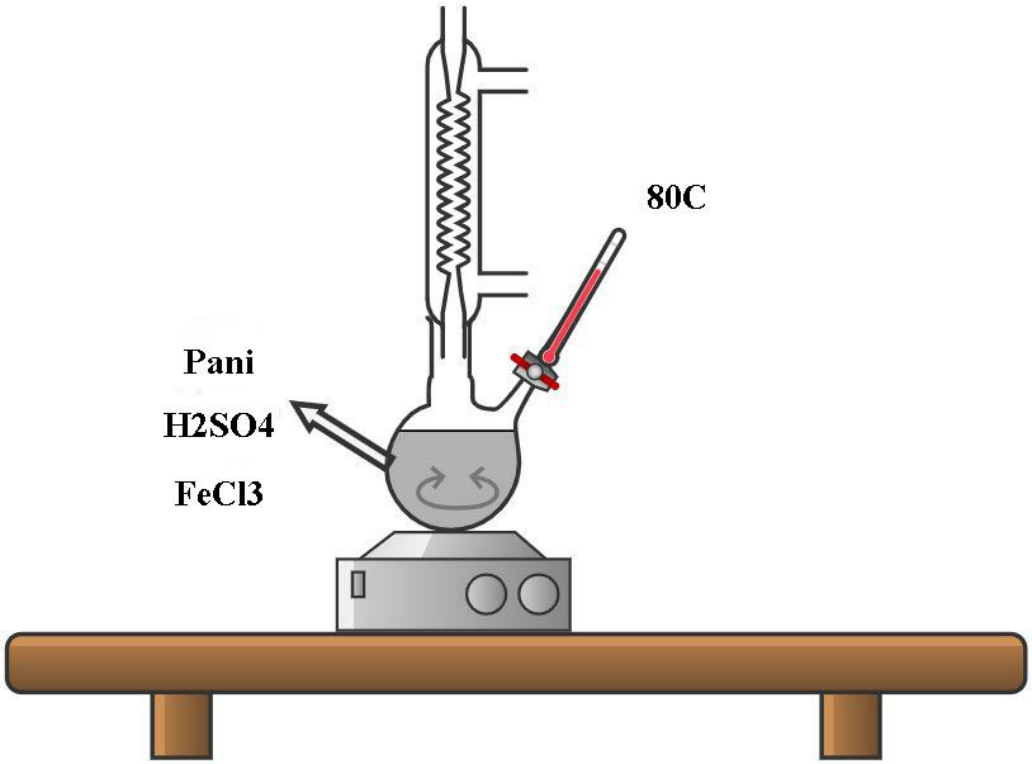


Figure 2.3 Synthesis of Polyaniline.

2.5 Production and characterization of button cell type Li-ion batteries

The prepared polypyrrole, polyaniline, heteroatom doped graphene oxide-based materials and fumed silica (7 nm particle diameter) will be mixed in different compositions to form composites and used as anode material in button type Li-ion batteries. The mixing ratios of the components to be used for the formation of the anode material are shown in Table 1.1. For the anode material, 0.45 g of active material will be prepared, and the binder ratio will be kept as 0.05 g (90:10). Polyvinylidine fluoride (PVDF) will be used as a binder. At this point, PVDF will

first be dissolved in 4 mL N-methyl pyrrolidine and after 15 minutes of stirring at 1250 rpm, the active substance will be added to the system and mixed for 20 minutes at 1250 rpm in a fume hood. The prepared mixture will be drawn on copper foil with a thickness of 120 microns, dried at 70 ˚C and cut circularly with a diameter of 16 mm to be placed in a CR2032 type button battery (Figure 3). The weight of the coating will be determined by weighing the blank and coated weight of the foil. The 0.75 mm thick Li foil to be used as cathode material will be cut circularly with a diameter of 16 mm. The anode and cathode materials to be prepared in this way will be separated from each other by means of a 25 micrometer thick polypropylene separator and 1.0M LiPF6 (in Ethylene carbonate: Dimethyl carbonate (EC:DMC) (1:1)) will be added to the battery at a rate of approximately 20% of its weight and the button battery system will be closed under pressure. The prepared battery will be kept for one day and then characterized by alternating voltammetry method with a scan rate of 0.5 mVs-1 in the range of 0.02 V to 3 V. In the electrochemical impedance spectroscopy method, electrochemical impedance spectra will be taken against open circuit potential at 5 mV amplitude voltage in the frequency range of 0.01 Hz to 10000 Hz and the raw data obtained will be adapted to the most appropriate equivalent circuit model and the solution resistance, charge transfer resistance, solid electrolyte interface resistance, double layer capacitance and Warburg impedance components will be examined. The prepared battery systems will be subjected to 10 cycles of charge-discharge at different C ratios (0.1C, 0.5C, 1.0C, 2.0C, 5.0C and 10C) and the initial and final specific capacities of the systems will be examined at 10C charge-discharge density for 100 cycles. The charge-discharge tests will be performed in the potential range of 0.02V to 3 V. With the help of the data obtained, the specific capacities of the batteries will be determined.

Table 2.1 All prepared batteries.

Sampels Code	N-GO %	S-GO %	Cl-GO %	Ppy-Pani %	Fumed silika %	PVDF %	Black Carbon
N0	**45**	**-**	**-**	**-**	**45**	**10**	**5**
S0	**-**	**45**	**-**	**-**	**45**	**10**	**5**
Cl0	**-**	**-**	**45**	**-**	**45**	**10**	**5**
N1-ppy	**20**	**0**	**0**	**55**	**10**	**10**	**5**
N2-ppy	**55**	**0**	**0**	**20**	**10**	**10**	**5**
S1-ppy	**0**	**20**	**0**	**55**	**10**	**10**	**5**
S2-ppy	**0**	**55**	**0**	**20**	**10**	**10**	**5**
Cl1-ppy	**0**	**0**	**20**	**55**	**10**	**10**	**5**
Cl2-ppy	**0**	**0**	**55**	**20**	**10**	**10**	**5**
N1-pani	**20**	**0**	**0**	**55**	**10**	**10**	**5**
N2-pani	**55**	**0**	**0**	**20**	**10**	**10**	**5**
S1-pani	**0**	**20**	**0**	**55**	**10**	**10**	**5**
S2-pani	**0**	**55**	**0**	**20**	**10**	**10**	**5**
Cl1-pani	**0**	**0**	**20**	**55**	**10**	**10**	**5**
Cl2-pani	**0**	**0**	**55**	**20**	**10**	**10**	**5**

2.6 Characterization Methods

Phase composition assessed using a Powder X-ray diffractometer. Cu Kα radiation with a wavelength of 1.54 Å was employed at 40 kV and 15 mA. The diffraction patterns were gathered between 10 and 90 degrees with an increment of 0.02 degrees. The analysis of the results was conducted using PDXL software by comparing them to the data in the library. The Zeiss EVO LS 10 instrument Scanning Electron Microscope (SEM) with an energy-dispersive spectrometer (EDS) was used to analyze the morphology, composition, and structure of the samples at various magnifications. The Quantachrome Corporation's Autosorb-6 device was used for BET analysis to calculate surface areas while the Perkin Elmer Spectrum One model equipment was used to record the chemical structure of electrodes with FT-IR spectra using the ATR technique. Elemental analyses were performed using a Perkin-Elmer 240C elemental analyser. Data from Thermogravimetric analysis (TGA) was gathered in a nitrogen environment, ranging from 21°C to 850°C, using a DTG thermo-analyser and a heating rate of 10 C/min. The Entek Electronic FPP470 model instrument was used to measure the electrical conductivity of electrodes using a 4-point method. Quantachrome Instrument was used to perform Brunauer-Emmett-Teller (BET) analyses. Furthermore, EIS tests were conducted with an Interface 1010B Potentiostat at different potentials, across a frequency range of 0.01 to 20,000 Hz, using a 5mV. The EIS spectrum was analyzed using two types of equivalent circuit model as shown in Figure 2.4 A and B.

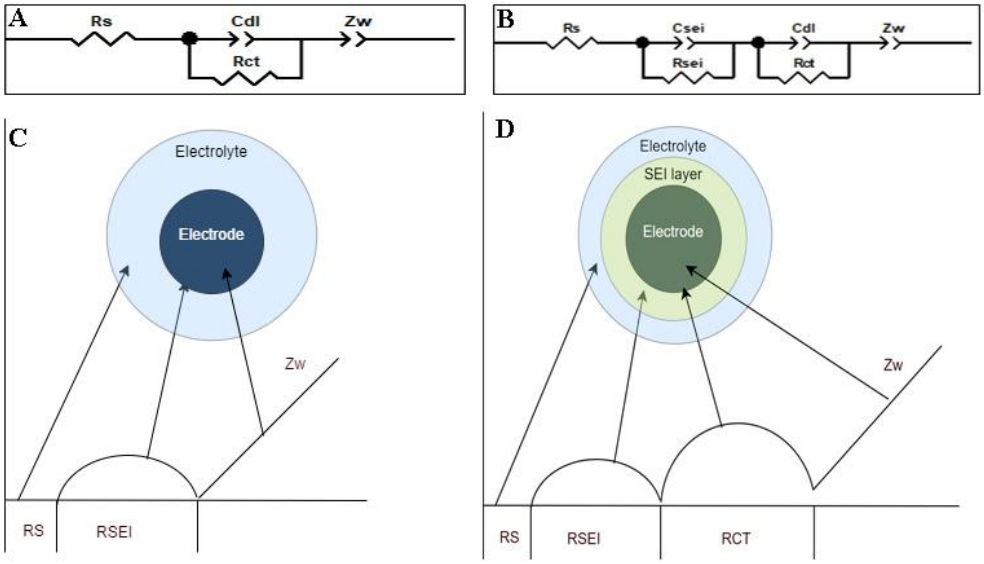


Figure 2.4 A) Equivalent circuit model of one semi-circle and B) Equivalent circuit model of two semi-circles.

3
RESULTS AND DISCUSSION

3.1 Characterazation of conducting polymer

3.1.1 Optimization of Polypyrrole synthesis

According to the electrical conductivity data presented in Figure 3.1 A, the sample PPy 0.3 had the lowest electrical resistance (high electrical conductivity) when compared to the other samples. Electrical resistance of the PPy decreased with increasing pyrrole concentration to the concentration of pyrrole 0.3 M, after this point resistance increased. Low monomer concentration leads to the creation of carboxyl defects caused by $FeCl_3$ overoxidation. In general, carbonyl defects can disrupt conjugation and perform as obstacles to charge transfer, reducing conductivity[65], [66]. Table 3.1 shows the surface areas of PPy 0.3 and PPy 0.5 were 7.69 and 8.26 g/cm^2, respectively. The morphologies of polypyrrole synthesized with (0.1, 0.3, and 0.5) M pyrrole concentrations were shown in Figure B, C, and D, respectively. The particles of PPy had spherical shape with good distribution in all concentration of pyrrole. According to these results, PPy 0.3 exhibited the highest electrical conductivity, smallest particle size, and favorable surface area. These attributes are advantageous for enhancing Li-ion battery performance, suggesting that PPy 0.3 may be considered the optimal sample among different pyrrole concentrations.

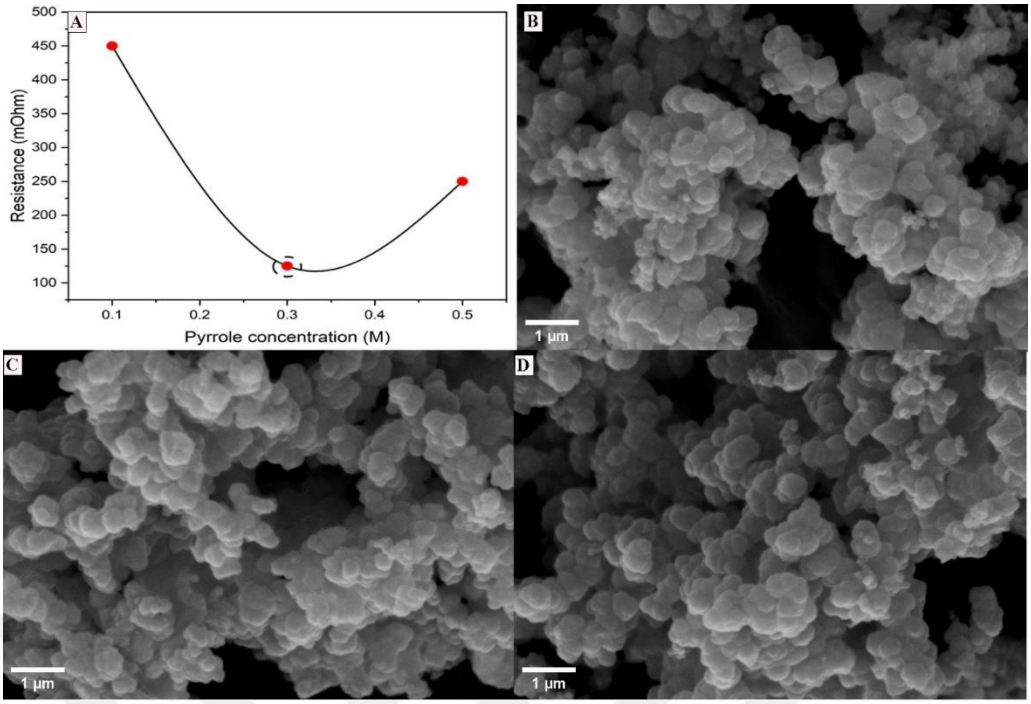


Figure 3.1 A) Electrical conductivity of polypyrrol at different monomer concentration, B) SEM image of Pyrrol 0.1M, C) SEM image of Pyrrol 0.3M, and D) SEM image of Pyrrol 0.5M

Table 3.1 Surface areas of polypyrrole prepared with different concentrations of pyrrole.

Test	**PPy 0.1 M - H_2SO_4-1M**	**PPy 0.3 M- H_2SO_4-1M**	**PPy 0.5 M - H_2SO_4-1M**
Surface Area (m^2/g)	**2.47**	**7.69**	**8.26**

In the second stage, optimization was conducted using various concentrations of H_2SO_4 while maintaining the pyrrole concentration at 0.3M. The results of electrical conductivity as shown in Figure 3.2 A. The sample prepared with 0.1 M sulfuric acid had less electrical resistance (high electrical conductivity) compared to other materials. With increasing H_2SO_4 concentration in the preparation of PPy, there were continuous decreases in the electrical conductivity of the materials. However, synthesis yielding of polypyrrole increased with increasing concentration of H_2SO_4. Surface area examination using BET reveals

that the samples PPy S0.1 and PPy S1 have the maximum surface area as shown in Table 3.2. Figure 3.2 C, D, E, and F describe the morphology of samples prepared with 0.1, 0.5, 3, and 5 M of sulfuric acid, respectively. This figure shows that particles have a spherical shape with good distribution in all pyrrole concentrations. However, PPy prepared with 0.5 M sulfuric acid had a bigger particle size, which agrees with the particle size analyses, and a small surface area.

Table 3.2 Surface areas of polypyrrole prepared with different concentration of sulfuric acid.

Test	**PPy 0.3 M H_2SO_4 0.1 M**	**PPy 0.3 M H_2SO_4 0.5 M**	**PPy 0.3 M H_2SO_4 1 M**	**PPy 0.3 M H_2SO_4 3 M**	**PPy 0.3 M H_2SO_4 5 M**
Surface Area (m^2/g)	**7.14**	**0.54**	**7.69**	**6.04**	**4.43**

Since the sample prepared with 0.3 M pyrrole and 0.1 M sulfuric acid had the highest electrical conductivity and high surface area, it was considered as the optimum sample. Successful synthesis of the plypyrrole was confirmed by FT-IR analyses (Figure 3.2 B). The peaks at 781 cm^{-1}, 933 cm^{-1}, 1036 cm^{-1}, 1176 cm^{-1}, 1300 cm^{-1}, 1458 cm^{-1} and 1531 cm^{-1} were related with C-H wagging vibrations, C–H out-of-plane deformation, C-H vibration of 2,5-substituted pyrrole, C-N bonds, C-H in-plane stretching, C-N stretching and pyrrole ring stretching, respectively. The peaks of pyrrole ring can also be seen at 1921 cm^{-1} and at 2100 cm^{-1} [66], [67].

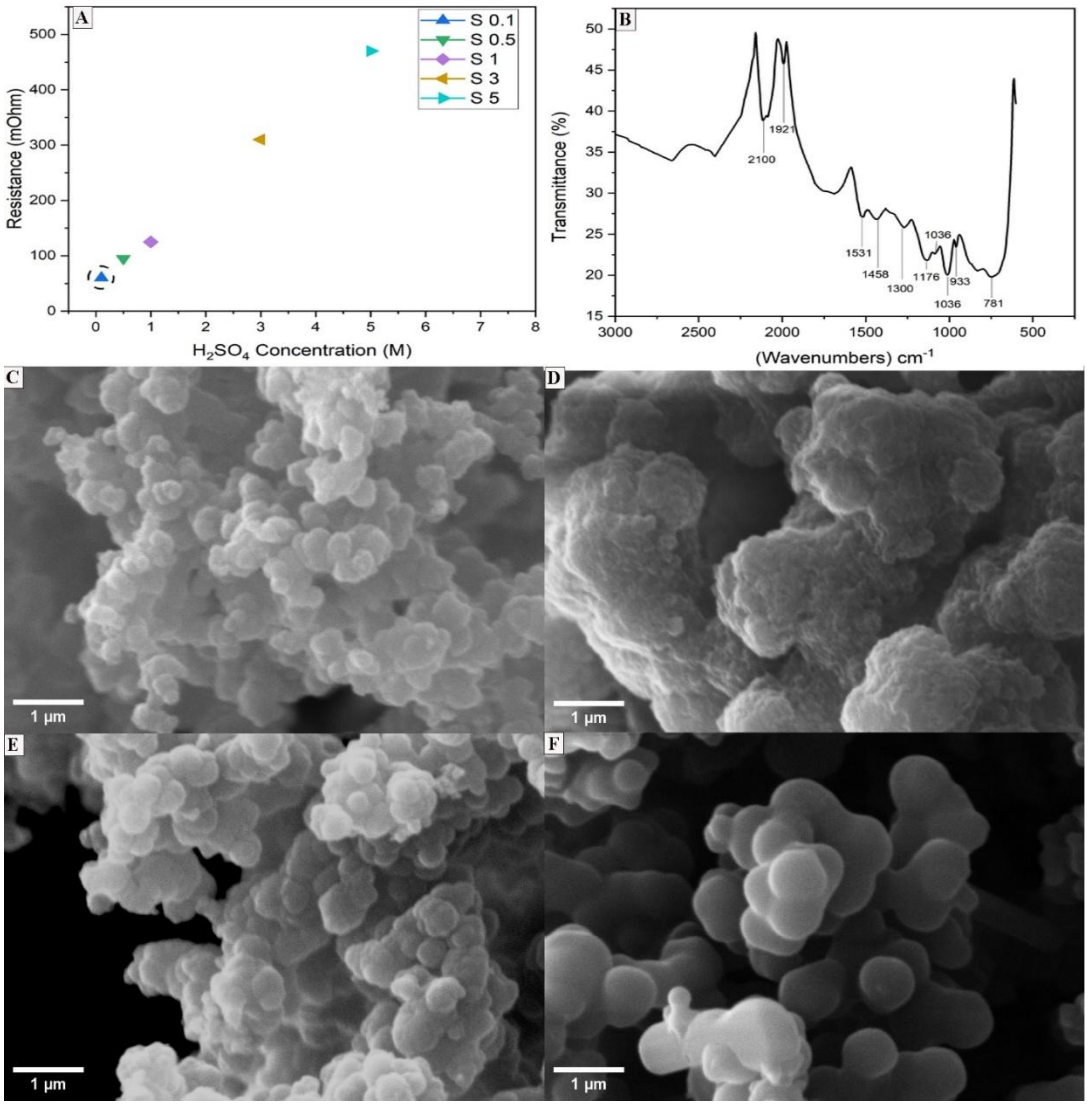


Figure 3.2 A) Electrical conductivity of polypyrrol at different acid concentration, B) FTIR of optimum polypyrrole C) SEM image of polypyrrole at 0.1M acid, C) SEM image of polypyrrole at 0.5M acid, and D) SEM image of polypyrrole 3M, and E) SEM image of polypyrrole 5M.

3.1.2 Optimization of Polyaniline synthesis

The concentration of aniline monomer is critical for increasing the electrical conductivity and surface area of synthetic polyaniline (PANI). Studies have shown that varying aniline concentration as in this article (0.1 M, 0.3 M, and 0.5 M) has a significant influence on the polymerization process and the resulting PANI properties. These results indicate that 0.3 M aniline has the highest electrical

conductivity and high surface area as shown in Figure 3.3 A due to optimal polymer chain growth and doping efficiency[68]. At this concentration, the polymerization process produces a well-defined nanostructured morphology with interconnected networks. At lower concentrations (0.1 M), insufficient monomer availability inhibits polymerization, resulting in shorter chains and lower conductivity and reducing surface area[69]. Higher concentrations (0.5 M) may cause excessive branching or aggregation, reducing transport charge. The balanced reaction kinetics of 0.3 M aniline result in well-structured PANI with enhanced π-conjugation and protonation levels, contributing to its superior performance[70]. The morphology shows good distribution of particles as in Figure 3.3 C, D, and E for pani 0.1, pani 0.3, and pani 0.5, respectively. The concentration of sulfuric acid (H_2SO_4) affects aniline polymerization, electrical conductivity, and surface area on polyanilne was studies at various H_2SO_4 concentrations (0.1 M, 0.5 M, 1 M, 3 M, and 5 M). The electrical conductivity and surface area improves up to 3 M due to improved protonation and doping efficiency and promoting the formation of a porous, fibrillar morphology that enhances surface area as shown in Fig.1B and Table 2[71]. Higher acid concentrations provide higher charge delocalization along the PANI backbone, which improves conductivity. At 5 M H_2SO_4, no solid PANI powder formed, due to high acid strength interrupting polymerization and hindering chain, resulting in incomplete reaction products[72]. The morphology also shows good distribution of particles as in Figure 3.3 F, G, and H for polyaniline at 0.1, 0.5, 3 M of acid respectively. The sample produced with 0.3 M aniline, and 3 M sulfuric acid was chosen as the optimal sample since it had the maximum electrical conductivity and surface area. FT-IR measurements confirmed the successful synthesis of polyaniline (Figure 3.3 I)[73][74].

Table 3.3 Surface area results of optimization synthesis for polyaniline.

Sample	Surface area m^2/g
Optimization of monomer Pani	
Pani 0.1-S1	**22,3075**
Pani 0.3-S1	**23,8030**
Pani 0.5-S1	**15,7651**
Optimization of Sulfuric acid	
Pani 0.3-S0.1	**23,5146**
Pani 0.3-S0.5	**18,9312**
Pani 0.3-S3	**32,5027**
Pani 0.3-S5	**There is no powder synthesized**

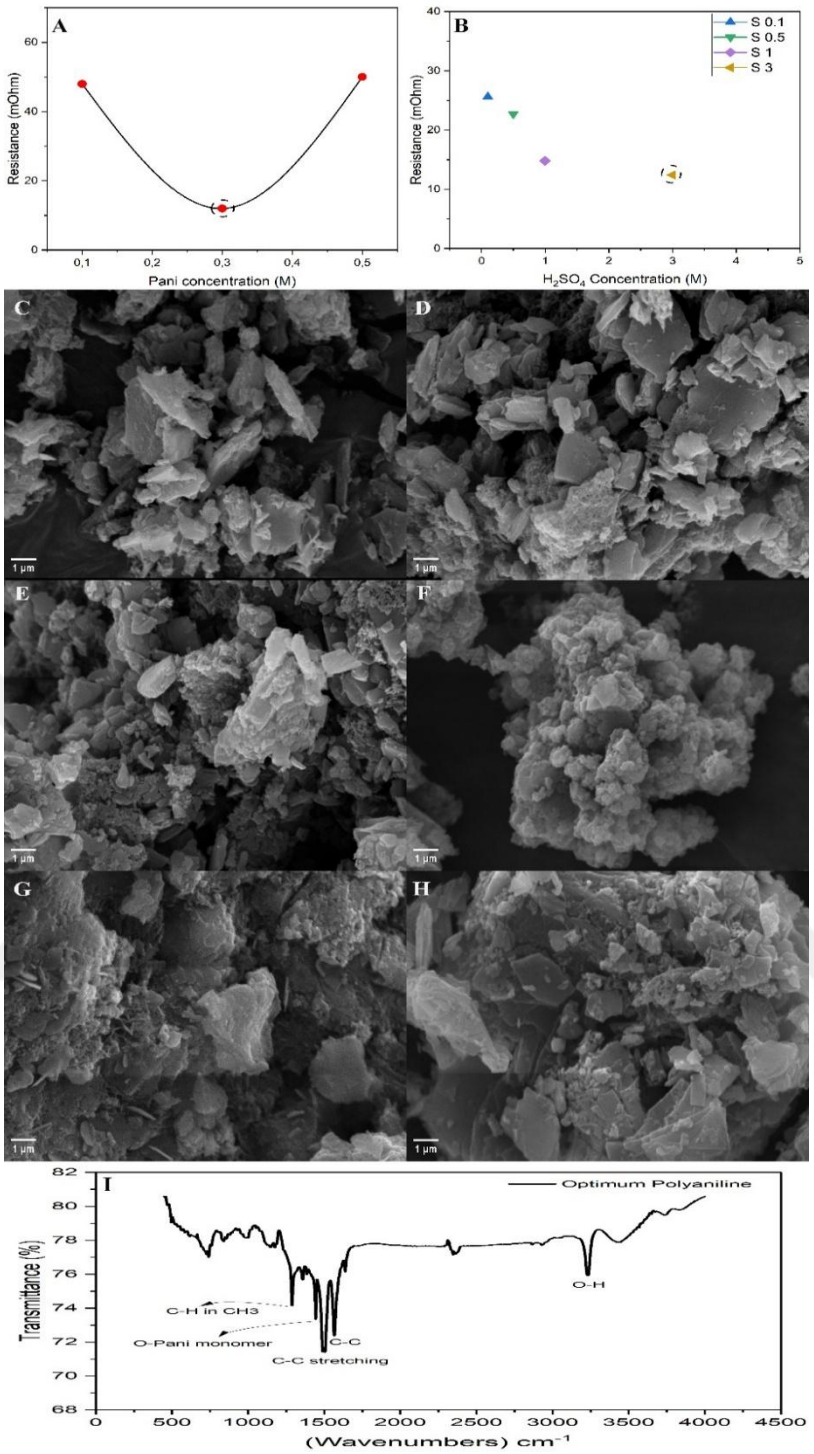


Figure 3.3 A) Electrical conductivity of Pani at different monomer concentration, B) Electrical conductivity of Pani at different acid concentration, C SEM image of PANI 0.1, D) SEM images of PANI 0.3, E) SEM images of PANI 0.5, F SEM image of PANI S0.1, G) SEM images of PANI S0.5, H) SEM images of PANI S3, and I) FTIR spectrum of optimum polyaniline sample.

3.2 Characterization of doped graphene oxide

Raman spectroscopy is a very versatile technique to detect the disordered structure of carbon and to determine the number of sp2-hybridized carbon rings. The D band (1350 cm-1) is related to the density of defects in the structure. The higher the intensity of the D band compared to G band is related to there being more defects in the structure of the graphene-based powders, and the presence of disorder. The G band (1580 cm-1) has E2g symmetry and is related to in-plane vibrations. The 2D peak (2700 cm-1) is used to interpret graphene quality, gain information about ring defects and provide information about the number of layers. The 2D peak becomes wider and shifts to the lower wavelength with an increasing number of layers. On the other hand, monolayer graphene has a sharper 2D peak at higher wavelength. It is observed that the G peak intensity decreases at lower wavelength in single layer graphene. With the increasing number of layers, the G peak shifts to lower wavelengths, and the ratio of G peak intensity to 2D peak intensity increases as shown in Figure 3.4. The average size of sp2 domain or cluster diameter, was calculated by Tuinstra and Koenig equation (TK) given in Equation (1):

$$ID/IG = C(\lambda)/ L\alpha \qquad (3.1)$$

The calculated graphene rings according to the Tuinstra and Koenig equation were given in Table 3.4.

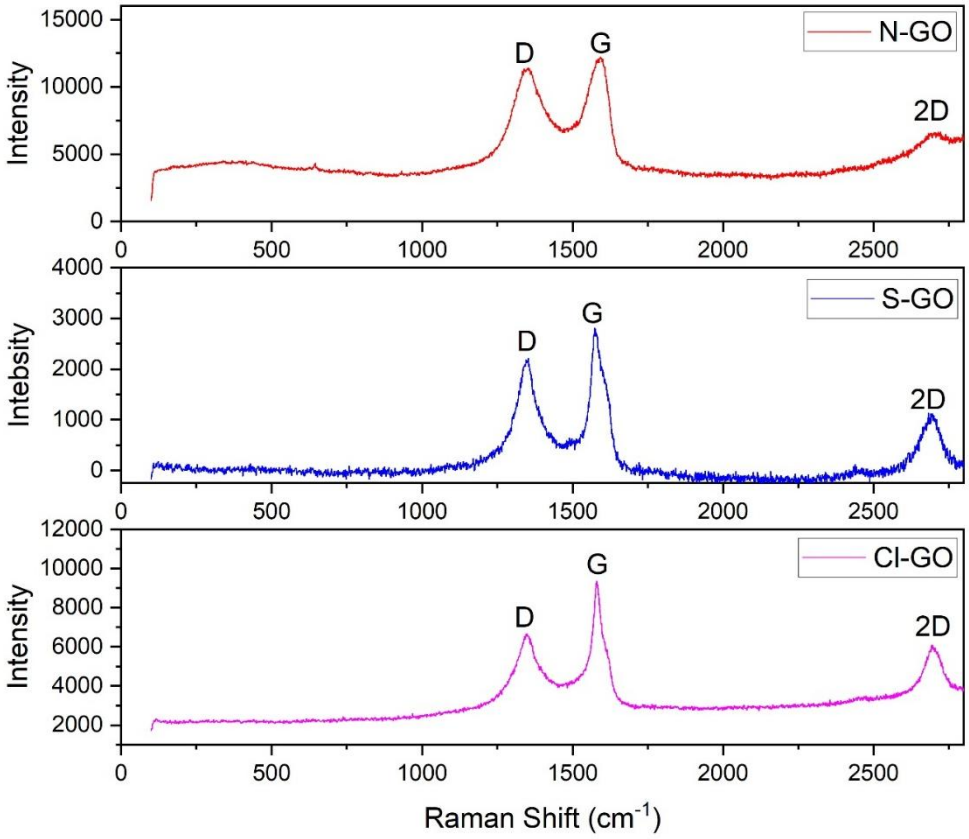


Figure 3.4 Raman spectra of N-GO, S-GO, and Cl-GO.

Table 3.4 Results of Raman analysis.

Sa.	B.D	B.G	B.2D	I.D	I.G	I.2D	ID/IG	IG/I2D	Lα (Å)	No. Rings
N-GO	1351	1592	2721	11402	12213	6641	0.93	1.8	47,3	18
S-GO	1352	1572	2695	2211	2813	1119	0.78	2.8	56.4	22
Cl-GO	1349	1580	2706	6664	9344	6098	0.71	1.5	61.8	24

As shown in Figure 3.4 and Table 3.4 the N doped graphene oxide (N-GO) has the highest ratio of (ID/IG) and lower number of rings (16) which means it contains a high defect size compared to S-GO and Cl-GO. This defect can create active sites for Li+ during operation of battery. The (G) band Cl-GO sample was shifted to lower wavelength and (D) band shifted to higher wavelength which indicated the chlorine doped graphene oxide has a few layers of graphene compared to N-GO and S-GO[75][76][77].

The chemical states of the elements are evaluated by X-ray photoemission spectroscopy (XPS) of N-GO (Figure 3.5). The (O 1s) spectrum could be deconvoluted into three subpeaks at 531.2, 532.3 and 533.5 eV (Figure 3.5 A), which could be attributed to the presence of different oxygen functionalities such as C= O, C-O, and O= C-O, respectively. Figure 3.5 B exhibits four peaks of the (C 1s) spectrum peaks centered at 284.5, 286.7 and 287.9 eV correspond to the sp2 C-C, C-N, C-O and C= O groups, respectively. The N 1s peak can be split into five individual peaks (as shown in Figure 3.5) located at 399.2 eV,401.4 eV, and 405.6 eV associated with pyridinic, graphitic and N-oxidized, respectively (as shown in Figure 3.6 the possible configurations of the nitrogen atoms). Each of these configurations affects the electronic and transport properties of the functionalized material rather differently[75][78].

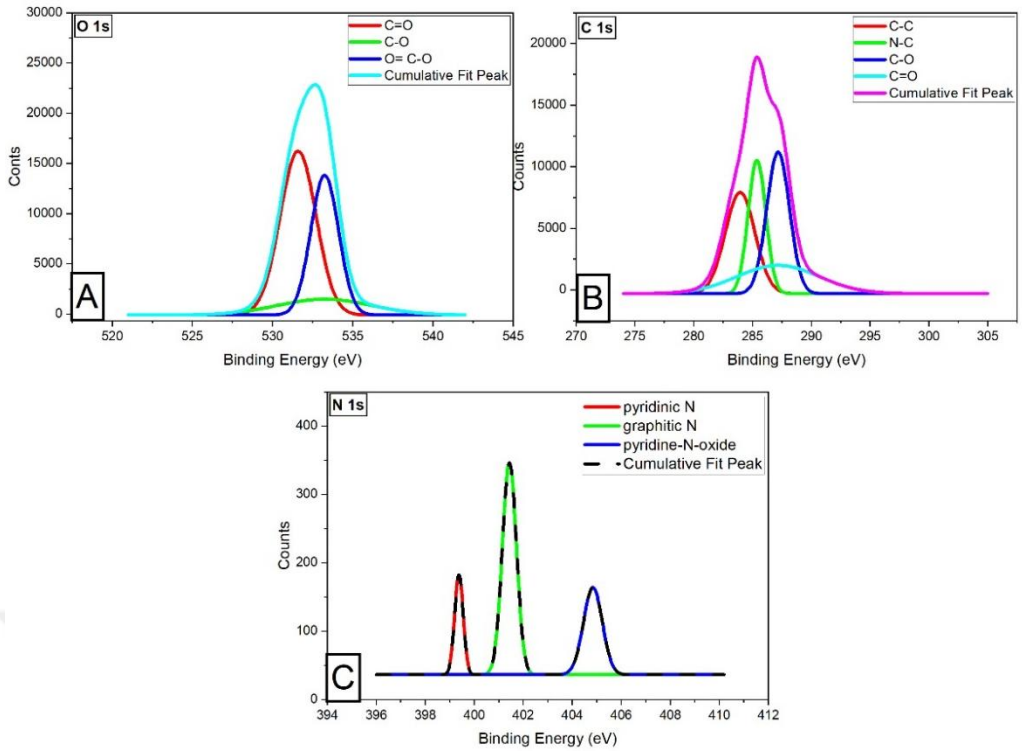


Figure 3.5 XPS spectra of N-GO, (A) O 1s, (B) C 1s and (C) N 1s.

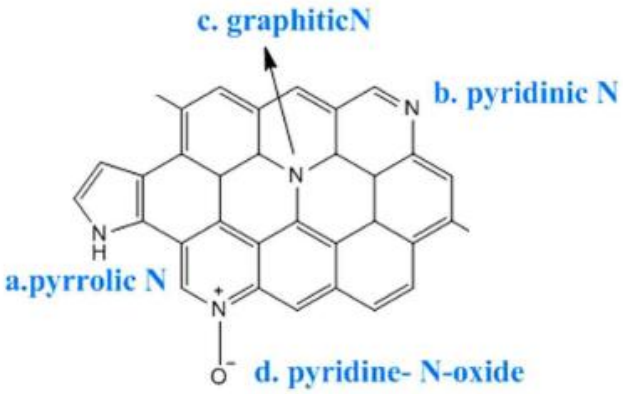


Figure 3.6 Common atomic configurations of nitrogen dopants in the graphene lattice.

Sulfur doped graphene oxide (S-GO): Chemical composition of the prepared sulfur-doped graphene powders was determined by XPS analysis. Figure 3.7 A, B and C show the C1s, S2p and O1s XPS spectra of S-GO. The peaks at around 284.6, 286.4, 287.1, and 288.3 eV was related to the formation of C-C, C-S, C═O, and O C═O, respectively (Figure 3.7 A). These results showed that the main surface of the graphenic layers consists of covalently bonded sulfur and oxygen atoms. When the S2p XPS spectra of the S-GO were analyzed (Figure 3.7 B), the formation of C- SOx -C (x: 2, 3) on the graphenic layers was determined.

O1s XPS spectra of S-GO (Figure 3.7 C) also supported the formation of –C═O, –C–O and –S–O with the corresponding peaks at around 531.2 eV, 533.3 eV and534.5 eV, respectively [76][43][79].

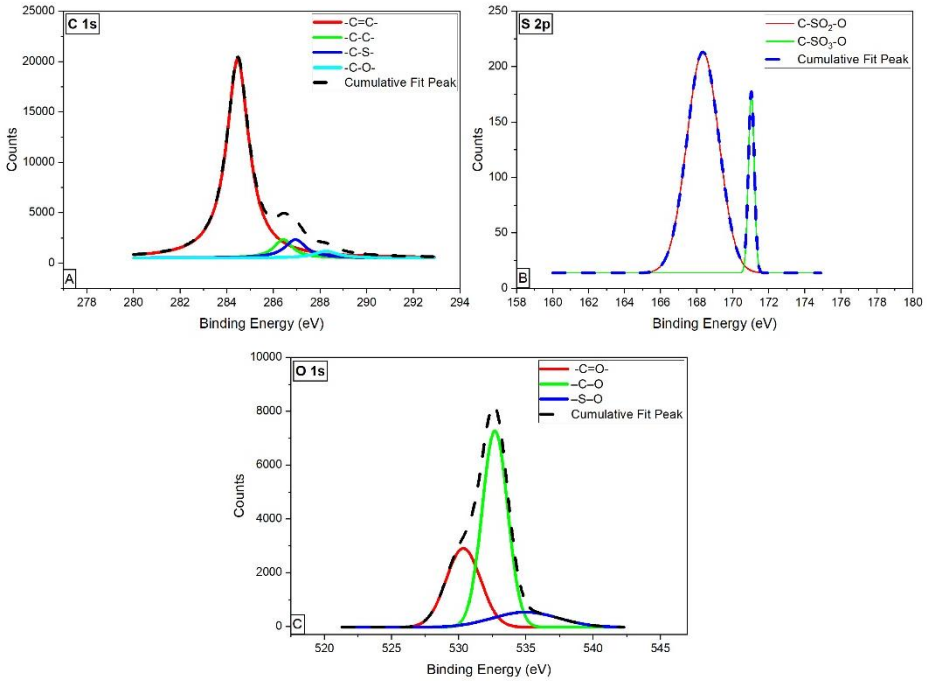


Figure 3.7 XPS survey spectra of the S-doped graphene; (A) C1s XPS spectra; (B) S 2p XPS spectra and (C) O1s.

Chlorine doped graphene oxide (Cl-GO): Chemical structure of Cl-GPGE's surfaces was analyzed by XPS analysis. Figure 3.8 A shows C1s XPS spectra of Cl-GO, peaks can be observed at around 284.5 eV, 285.93 eV, and 286.6 eV for –C–C–, –C–Cl, and C–Cl bonds, respectively. Cl2p XPS spectra of Cl-GO were shown in Figure 3.8 B, peaks of Cl–O, —ClO3 and —ClO4 can be seen at 206.2,207.1 and 209.6 eV, respectively. The O 1s spectra of graphene-based powders are given in Figure 3.8 C, peaks at 531.7, 532.26 and 534.4 eV were determined for C═O, –C–O and –O═C–O, respectively.

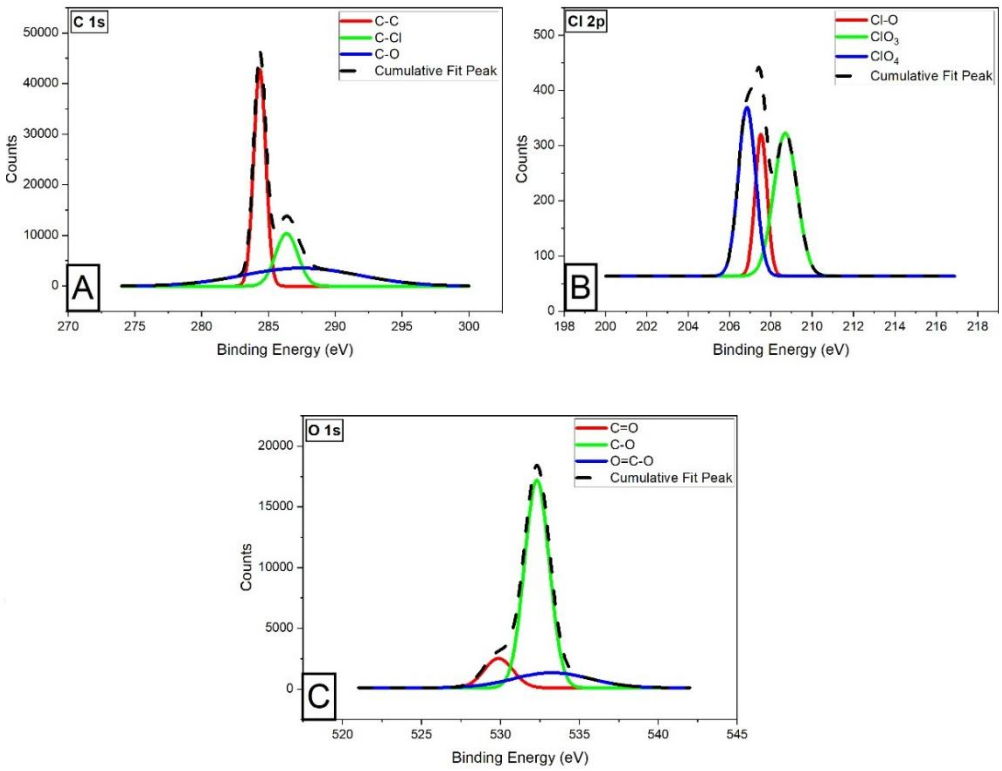


Figure 3.8 XPS survey spectra of the Cl-doped graphene; (A) C1s XPS spectra; (B) Cl2p XPS spectra; (C) O1s XPS spectra.

BET of N-GO, S-GO, and Cl-GO were shown in Table 3.5 show the surface areas of doped graphene oxide and show the N-doped graphene oxide was the highest surface area among the other doped graphene oxide. SEM and TEM of N-GO, S-GO, and Cl-GO were shown in Figure 3.9 The multilayer graphene in SGO tended to consolidate, resulting in larger clusters. The ultrathin graphene layers, exhibited high transparency, showed both wrinkled and laminar structures, with graphene nanosheets tending to aggregate and form clusters.

Table 3.5 Surface area of doped graphene oxide.

Sample	Surface Area m^2/g
N-GO	**110.7**
S-GO	**16.1**
Cl-GO	**23.4**

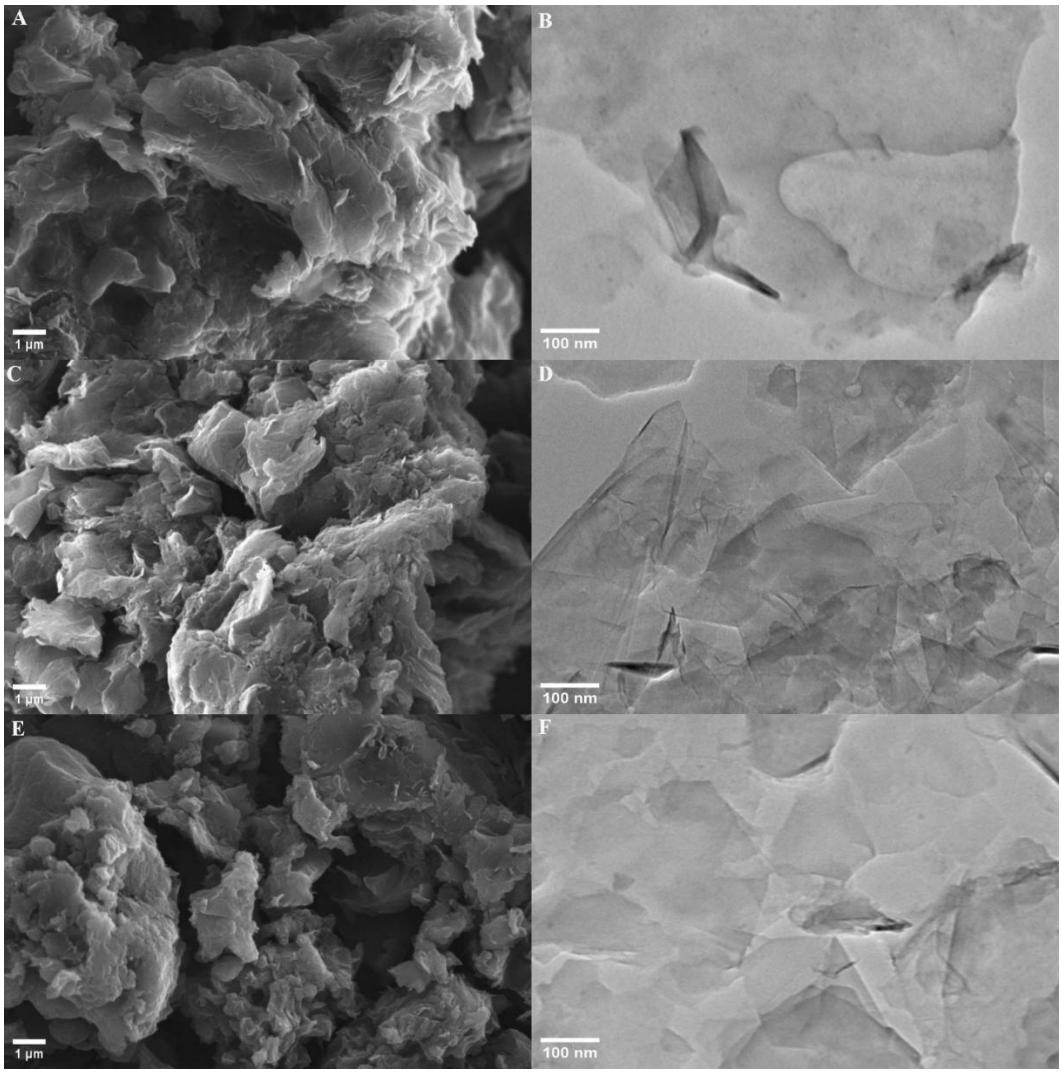


Figure 3.9 Morphology of doped graphene oxide, (A) SEM of NGO, (B) TEM of NGO, (C) SEM of SGO, (D) TEM of SGO, (E) SEM of ClGO, and (F) TEM of ClGO.

3.3 Electrochemical measurements

3.3.1 Reference samples (doped graphene oxide and fumed silica)

The cyclic voltammograms in Figure 3.10 show that the three anode materials have same CV characteristics. The CV curves show distinct reduction (cathodic) and oxidation (anodic) peaks, representing the lithiation (discharge) and delithiation (charging) processes, respectively. These peaks indicate reversible electrochemical processes happening in the composite material during Li-ion insertion and extraction. The first cycle frequently exhibits irreversible reactions due to the creation of the solid-electrolyte interphase (SEI) layer, which is typical in anode materials. The variations between the reduction and oxidation peaks in the first and second cycles demonstrate this irreversibility. The CV curve tends to stabilize in the second cycle, indicating that the composite material's reversibility and electrochemical stability have improved since its initial SEI production. The galvanostatic charge-discharge (GCD) curves for SiO_2 composites with N-, S-, and Cl-doped graphene oxide (GO) anodes have been investigated at various current rates to determine the electrochemical performance, including capacity, reversibility, and rate capability. The GCD profiles give significant details on the Li-ion storage behavior of these composite materials. All composites show typical charge/discharge plateaus, which correspond to Li-ion insertion/extraction processes. The plateaus become more apparent at lower current rates (e.g., 0.1C), showing well-defined redox processes. The N-doped GO composite (N-GO/SiO_2) shows more distinct plateaus, indicating a higher Faradaic contribution. This is likely owing to increased conductivity and Li-ion binding sites introduced by nitrogen doping. In the first few cycles, the discharge capacities (Li-ion insertion) exceed the charge capacities (Li-ion extraction), as is common owing to the creation of solid-electrolyte interphase (SEI) and irreversible processes. At low current rates (e.g., 0.1C), the S-GO/SiO_2 composite has a modest capacity, whereas the N-GO/SiO_2 composite has a larger capacity, possibly due to nitrogen's potential to increase electronic conductivity and supply extra active sites. The Cl-GO/SiO_2 composite has low-capacity values comparable to those of S- and N-doped composites, indicating that chlorine doping provides a balance of capacity and kinetics but not like sulfur and nitrogen. As the current rate increases (e.g., from 0.1C to 0.5C, 1C, etc.), all composites show capacity fading, which is predicted

owing to kinetic limits at higher current levels. The N-GO/SiO_2 composite preserves capacity better at greater rates, indicating enhanced rate capability, possibly due to nitrogen's effect on charge transfer. The S-GO/SiO_2 composite exhibits more capacity loss at higher rates, probably because to slower ion diffusion or weaker conductivity. The Cl-GO/SiO_2 composite has an intermediate rate performance, indicating that Cl doping enhances kinetics relative to S but not as much as N.

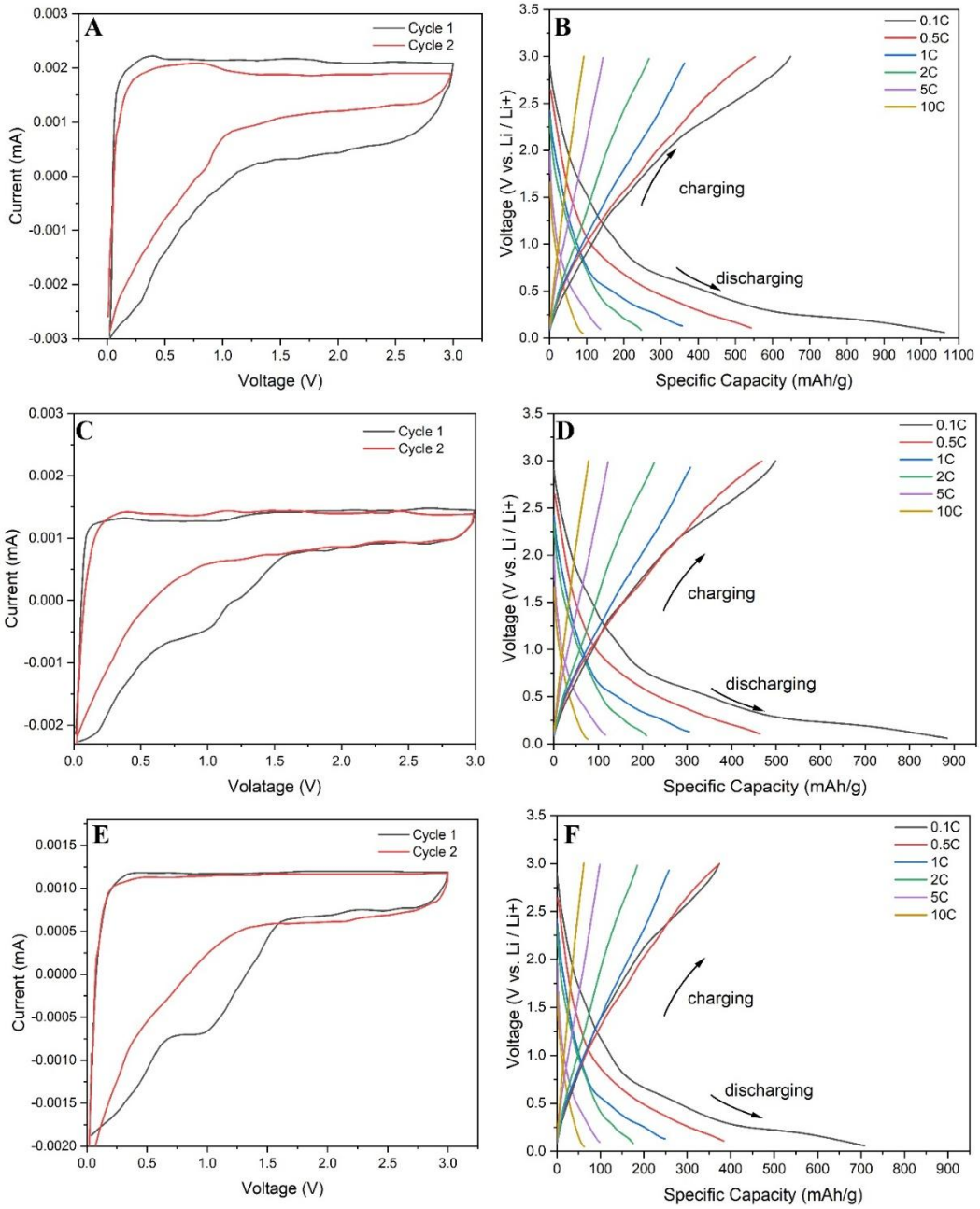


Figure 3.10 CV and charge-discharge at different rates, (A) CV of NGO, (B) Charge-discharge of NGO, (C) CV of SGO, (D) Charge-discharge of SGO, (E) CV of ClGO, and (F) Charge-discharge of ClGO.

Figure 3.11 A, C, and E show the cycling performance of reference samples (N-doped, S-doped, and Cl-doped) which shows the N-doped is higher performance compared to another doped samples, but the retention capacity is considered poor for all samples after 100 cycles at high current rate (10C). Figure 3.11 B, D, and F show the EIS test which also indicates the N-doped has lower resistances compared to other doped systems which also prove the good cyclability of N-doped. The

superior electrochemical performance of the N-doped graphene oxide can be attributed to the unique role of nitrogen heteroatoms in enhancing lithium-ion storage behavior. Nitrogen doping effectively modulates the electronic structure of graphene by introducing pyridinic, pyrrolic, and graphitic N sites, which increase electrical conductivity, create additional electrochemically active sites, and strengthen Li^+ adsorption, resulting in improved capacity and cycling stability. In contrast, Cl-doped graphene oxide shows the weakest electrochemical behavior among the samples studied, likely because chlorine doping mainly introduces structural defects and surface functional groups without significantly improving conductivity or lithium storage energetics, which can also promote side reactions and capacity fading.

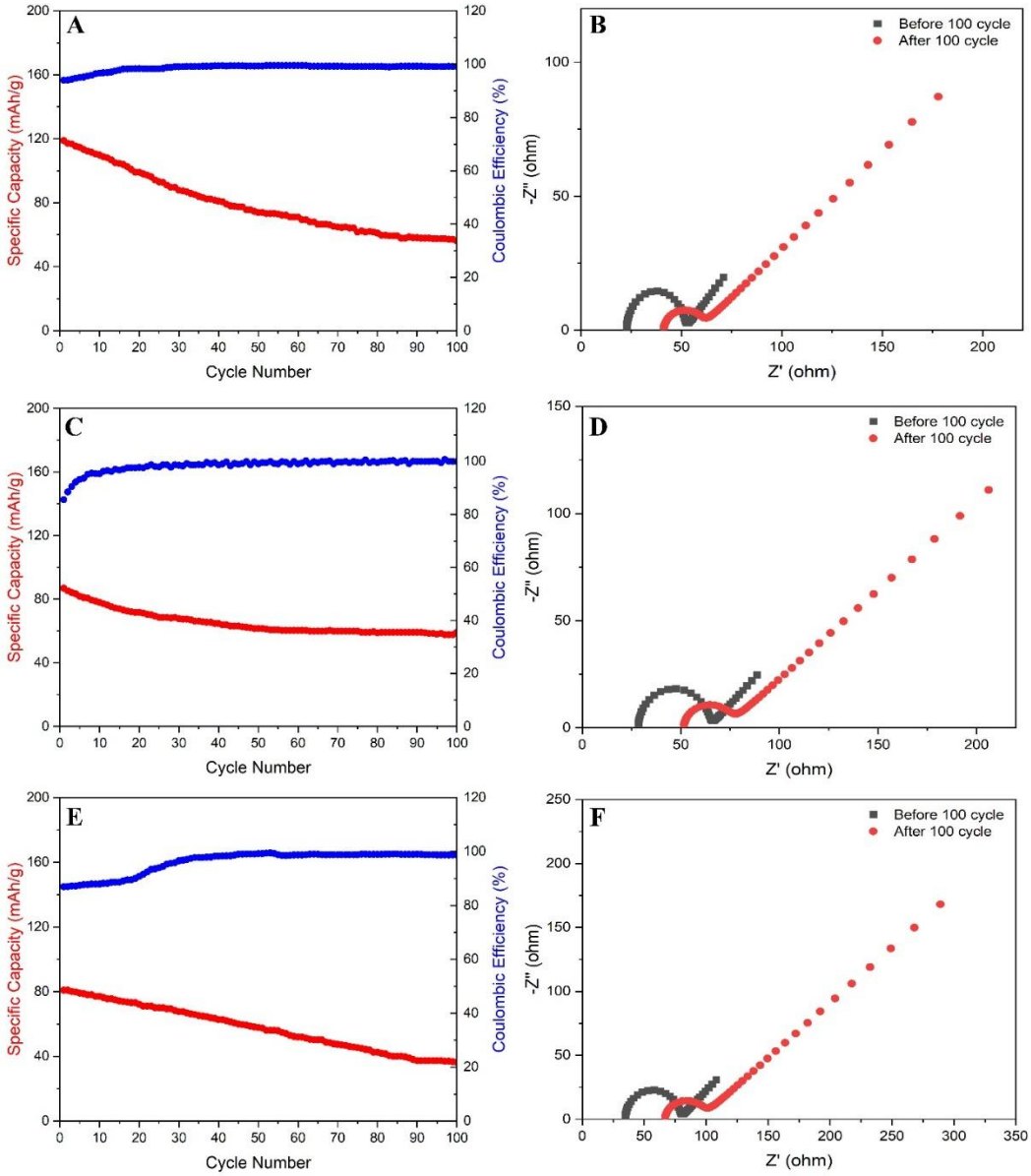


Figure 3.11 Cycling performance and EIS of doped graphene oxide, (A) Cycling performance of NGO, (B) EIS of NGO, (C) CV of SGO, (D) Cycling performance of SGO, (E) EIS of ClGO, and (F) Cycling performance of ClGO.

3.3.2 Polypyrrole samples

In Figure 3.12, cyclic voltammetry curves are tested between 0.01 to 3 V under 0.5 mV/s scan rate. Cyclic voltammograms of all samples highlighted the high reversibility level of the reactions of Li intercalation. Cyclic voltammograms are also closely identical with a typical CV curve for carbonaceous materials pointing. The first and second cycle for all samples is very identical which mean high stability of structure for samples[80][81].

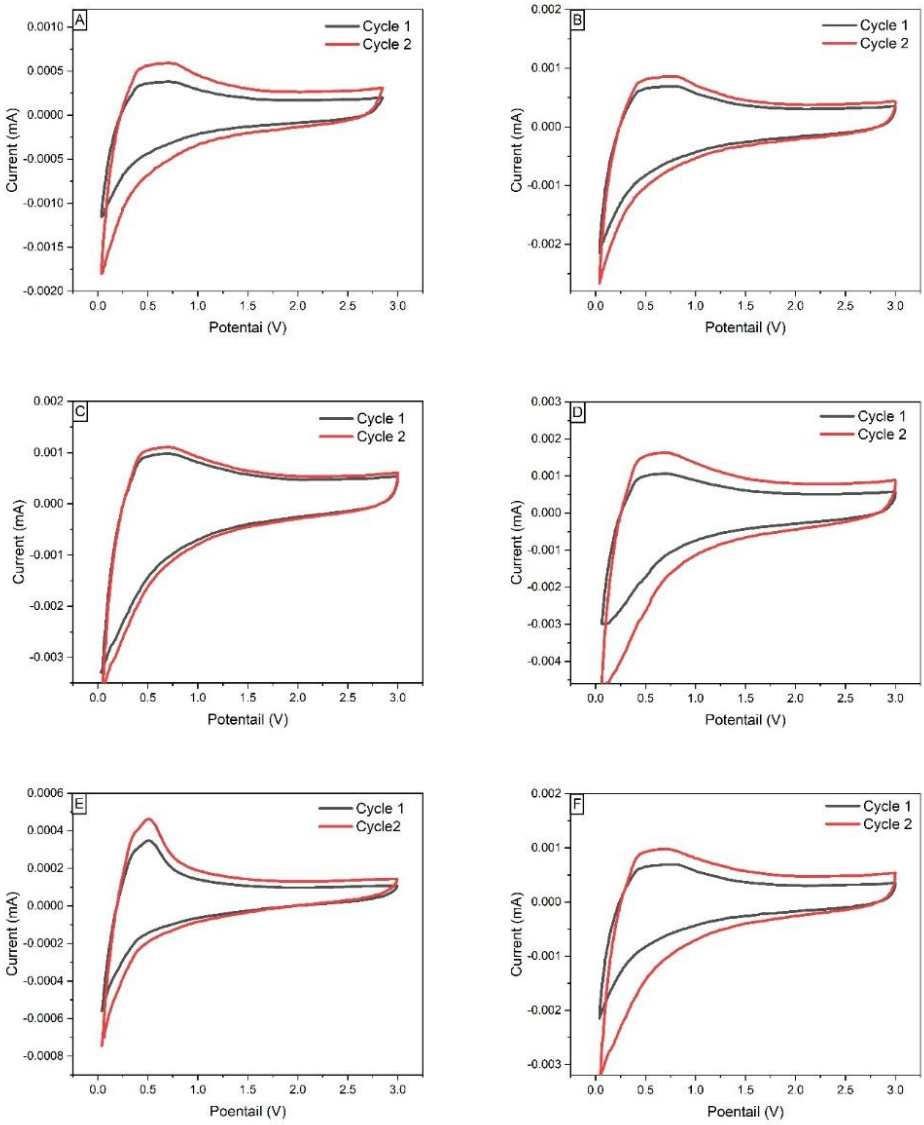


Figure 3.12 Cycling voltammetry of samples, (A) N1-ppy, (B) N2-ppy, (C) S1-ppy, (D) S2-ppy, (E) Cl1-ppy, and (F) Cl2-ppy.

Figure 3.13 A–F show the galvanostatic charge–discharge profiles of N-, S-, and Cl-doped graphene oxide/fumed silica composites in which polypyrrole (PPy) is used as the conducting polymer, evaluated at current rates from 0.1C to 10C. All PPy-based composites exhibit typical sloping charge–discharge curves without distinct voltage plateaus, indicating a combination of diffusion-controlled lithium intercalation and surface-controlled pseudocapacitive processes. At low current density (0.1C), relatively high specific capacities are observed for all dopant systems. However, compared to the references samples the capacity at low current

because the doped graphene oxide and silica have higher capacity compared with polypyrrole, the graphene oxide have high theoretical capacity (744 mAh/g)[82][83], theoretical capacity of polypyrrole is (72 mAh/g)[84], and for fumed silica is (1950 mAh/g) . However, the PPy-containing electrodes display more discharge capacity as the current rate increases, particularly at 5C and 10C. This behavior suggests slower charge-transfer kinetics and limited ion transport within the PPy matrix under fast charge–discharge conditions. The effect of amount of polypyrrole shows at high current which shows the samples with high content of polyapyrrole has excellent capacity at high current. Among the dopants, the N-doped graphene oxide composites (Figure 3.13 A and B) deliver the highest capacities and the most stable charge–discharge profiles across all rates, reflecting the beneficial role of nitrogen-induced conductivity enhancement and strong lithium-ion affinity. The S-doped composites (Figure 3.13 C and D) show moderate rate capability with increased voltage hysteresis, while the Cl-doped samples (Figure 3.13 E and F) exhibit comparatively lower capacities and faster capacity decay at high current density. Overall, although PPy improves the electrochemical activity of doped graphene oxide compared to polymer-free reference samples, which can be attributed to the lower intrinsic electrical conductivity, reduced structural stability, and less efficient redox reversibility of PPy during high-rate cycling as shown in Figure 3.14. These results highlight that the choice of conducting polymer plays a crucial role in determining the high-rate performance of doped graphene oxide composite anodes. Figure 3.15 shows the cycling performance ofor 100 cycles at high current rate (10C) wich is domenstrated the effect of polypyrrole for all sample dopant that have high content of polypyrrole show better performance than low content of polypyrrole.

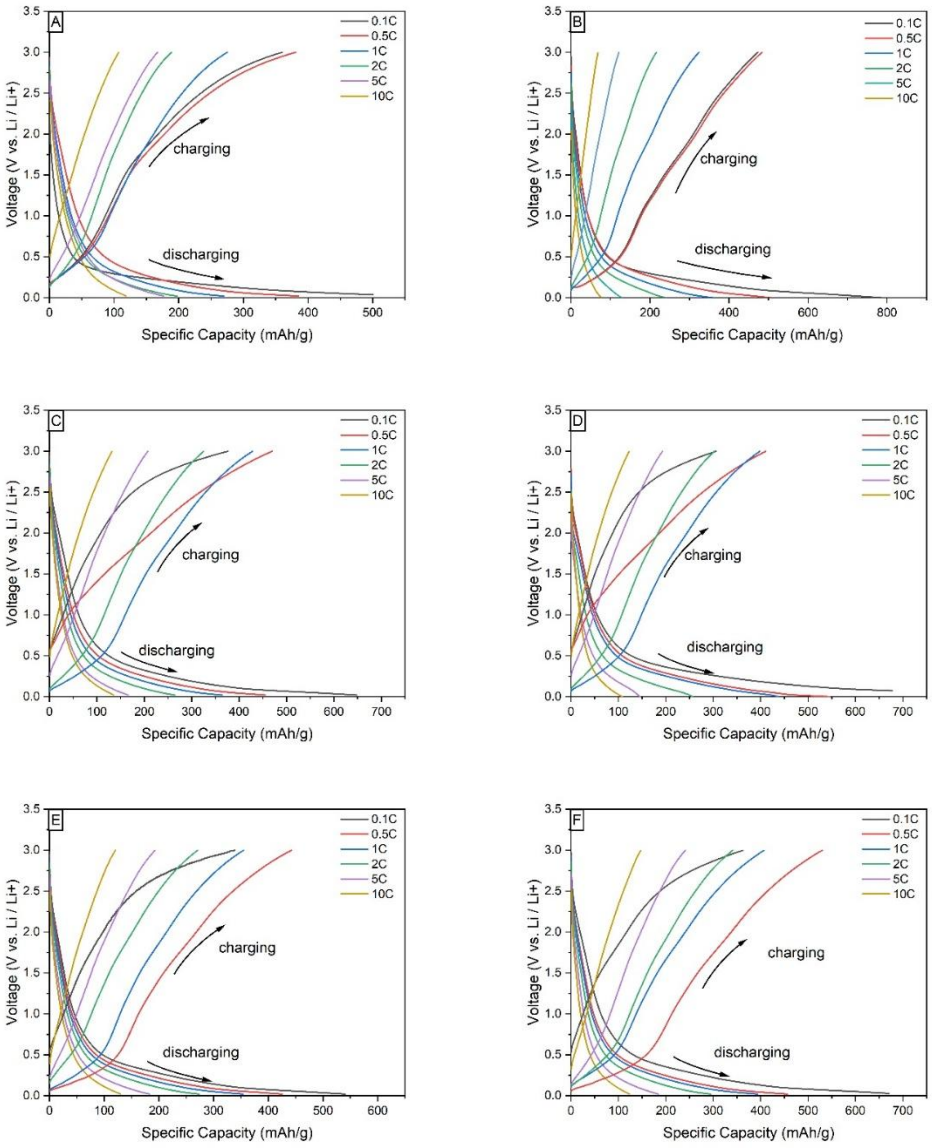


Figure 3.13 Charge-discharge at different rates of samples, (A) N1-ppy, (B) N2-ppy, (C) S1-ppy, (D) S2-ppy, (E) Cl1-ppy, and (F) Cl2-ppy.

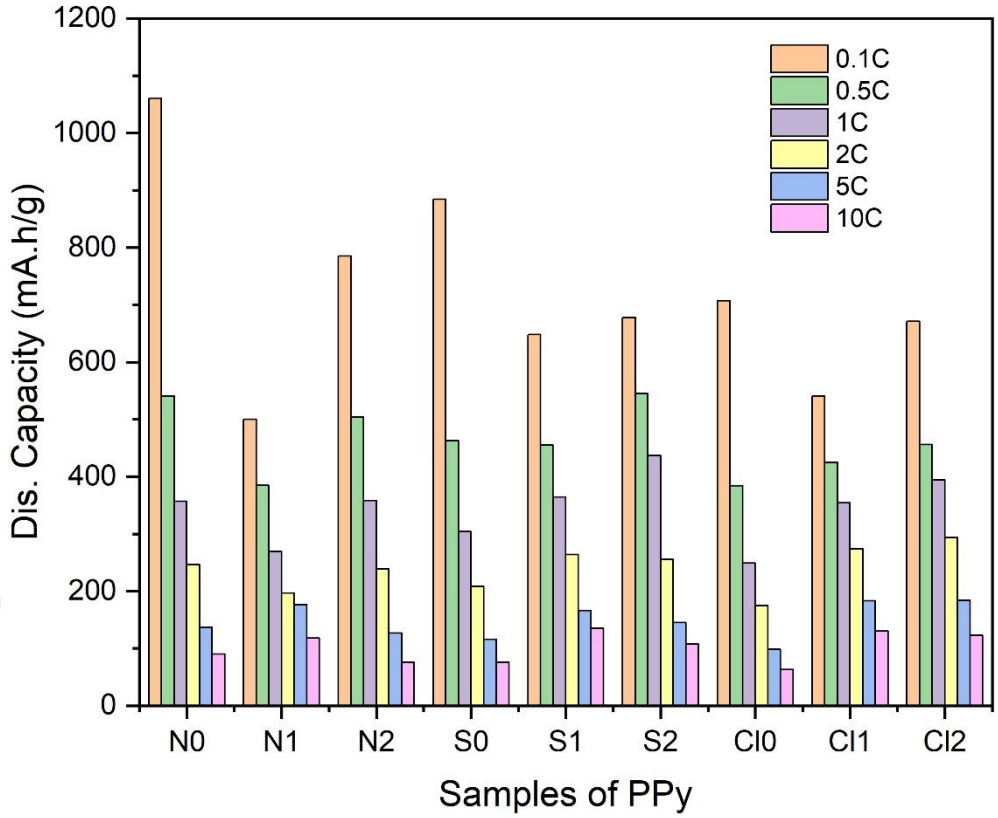


Figure 3.14 Comparasion of discharge capacity of polypyrrole samples.

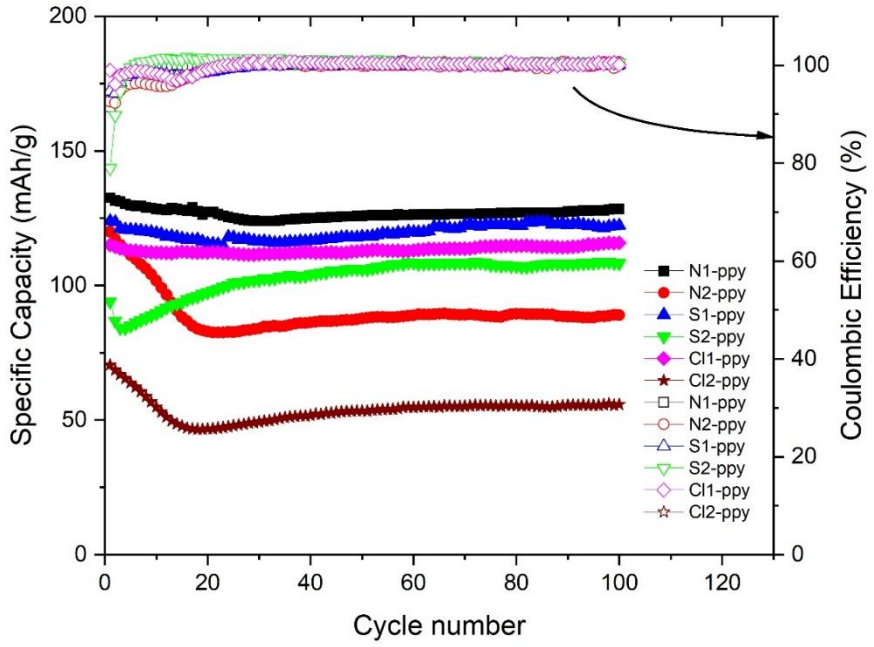


Figure 3.15 Cycling performance of ppy samples.

EIS measurements were conducted for half-cells before and after 100 cycles of charge and discharge. In the initial Nyquist plots obtained after cell assembly, a semicircle representing charge transfer resistance of electrode was observed. However, after 100 charge-discharge cycles, a second semicircle appeared, which is attributed to the formation of the SEI layer at the electrode-electrolyte interface. [85]. Figure 3.16 A, C, and E for samples high ratio of polypyrrole shows less resistance than samples of low ratio of polypyrrole which is reflected in a good cycling performance at high current and a proof of role for polypyrrole in li ion batteries. The superior electrochemical performance of the N-doped graphene oxide–polypyrrole–fumed silica composite, particularly at a low polypyrrole (PPy) ratio, can be attributed to the synergistic effects of nitrogen heteroatom doping and optimized polymer content. Nitrogen doping introduces abundant electrochemically active defect sites (pyridinic and graphitic N) and enhances electronic conductivity, thereby facilitating faster charge transfer and improved Li^+ adsorption and diffusion during lithiation/delithiation processes. In contrast, sulfur-doped graphene oxide exhibits moderate performance enhancement due to lattice distortion and increased interlayer spacing induced by the larger sulfur atoms, which can promote Li^+ diffusion but provide a less pronounced improvement in electronic conductivity compared to nitrogen doping. Chlorine-doped graphene oxide shows the lowest electrochemical performance among the studied dopants, likely due to weaker electronic interaction with the carbon framework and less effective contribution to charge carrier density. Furthermore, for all doped systems, composites with a low PPy ratio demonstrate better electrochemical behavior than those with a high PPy content, indicating that excessive PPy can dilute active material content, block lithium-ion transport pathways, and increase internal resistance. At optimized low concentrations, PPy acts as a conductive binder that improves electrical connectivity and buffers structural stress without hindering ion diffusion. These findings are consistent with previous reports on heteroatom-doped graphene/conducting polymer composites, confirming that both dopant chemistry and polymer loading play critical roles in determining the electrochemical performance of lithium-ion battery anodes.

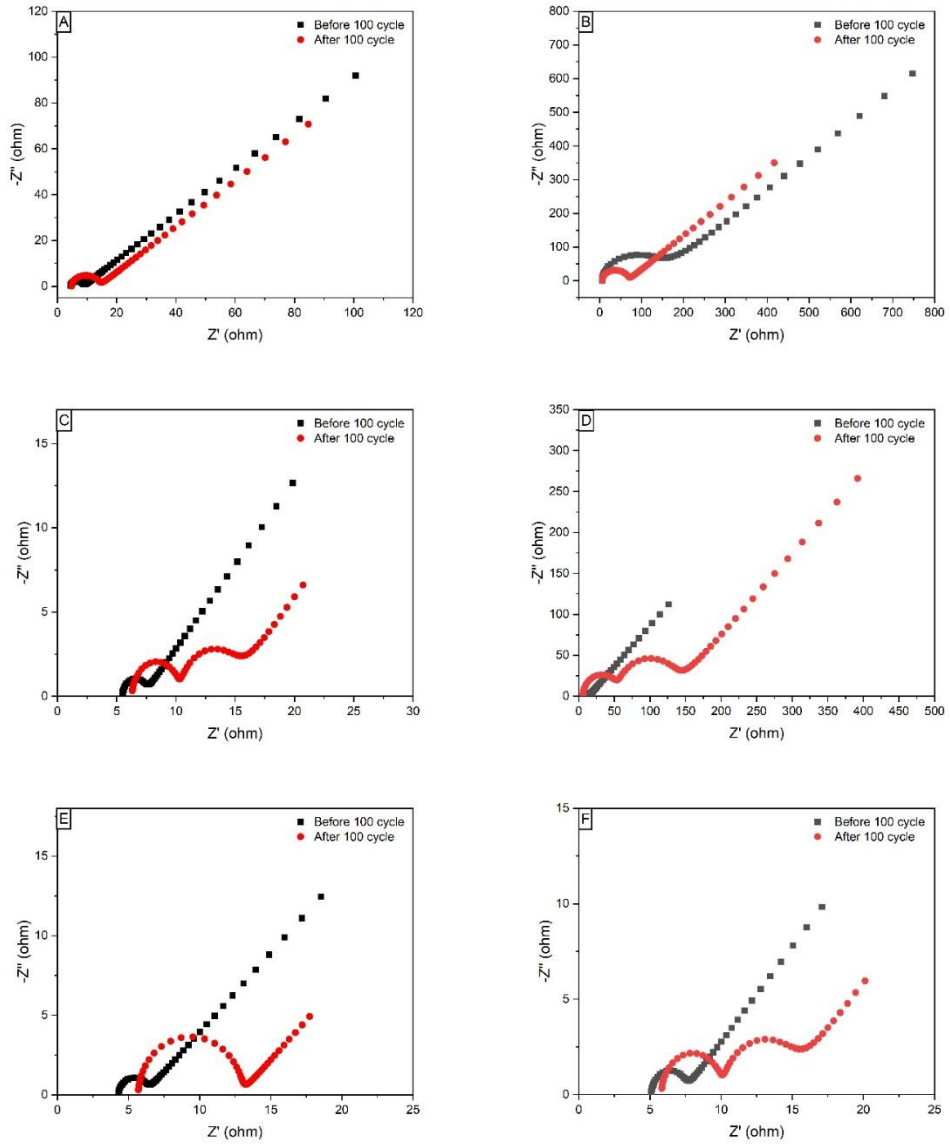


Figure 3.16 EIS of samples, (A) N1-ppy, (B) N2-ppy, (C) S1-ppy, (D) S2-ppy, (E) Cl1-ppy, and (F) Cl2-ppy.

Table 3.6 Resistancs values form EIS before and after cycling of polypyrrole samples.

Sample	R_s (Ω)	R_{SEI} (Ω)	R_{ct} (Ω)	W_z
N1-ppy before cycling	**4.394**	**-**	**4.266**	**30.7E-03**
N1-ppy 100 cycles	**4.816**	**-**	**9.139**	**39.9E-03**
N2-ppy before cycling	**6.028**	**-**	**131.7**	**0.916E-03**
N2-ppy after 100 cycles	**6.002**	**-**	**60.85**	**8.05E-03**
S1-ppy before cycling	**5.438**	**-**	**1.75**	**70.5E-03**
S1-ppy after 100 cycles	**5.112**	**1.429**	**0.706**	**71.0E-03**
S2-ppy before cycling	**5.791**	**-**	**8.044**	**25.1E-03**
S2-ppy after 100 cycles	**5.646**	**46.33**	**73.95**	**10.6E-03**
Cl1-ppy before cycling	**4.252**	**-**	**1.83**	**71.6E-03**
Cl1-ppy after 100 cycles	**5.671**	**-**	**7.15**	**181E-03**
Cl2-ppy before cycling	**4.9**	**-**	**1.623**	**59.7E-03**
Cl2-ppy after 100 cycles	**5.795**	**4.279**	**4.122**	**151E-03**

3.3.3 Polyaniline samples

Cyclic voltammetry was performed on the electrodes of pani samples to determine their electrochemical behavior and redox reversibility. The CV curves were taken between 0.02 and 3 V (vs. Li^+/Li) at a scan rate of 0.5 mV s^{-1} for the first two cycles, as shown in Figure 3.17 for samples. Cyclic voltammetry reveals electrochemical behavior during the initial cycles, which is crucial for understanding the creation and stability of the solid electrolyte interphase. The degradation of the electrolyte and the formation of the SEI layer occur at a broad peak of about 0.5 V, as seen in 3.17 B much broader, less discernible peak appears at 1.5 V, indicating a reaction between electrolyte and electrode and the beginning of SEI formation. This peak is more noticeable in low pani ratio for all doping elements in the first cycle than in high pani ratio, implying that SEI formation occurs primarily during the first cycle and that these initial reactions are irreversible[86]. The stability of this SEI, however, varies significantly amongst the composites. Reference samples (N0, S0, and Cl0), made up of doped graphene oxide and silica only, had the largest electrolyte breakdown, resulting in a thick and unstable SEI. This is demonstrated by its huge, wide cathodic peak and the considerable change in the next cycle. While samples contain pani have strong reversibility between the first and second cycles due to their polyaniline content, there is a clear performance hierarchy. Samples with high ratio of doped graphene to polyaniline, have a higher synergistic effect. This ideal equilibrium produces a persistent, passivating SEI, which is supported by N2-pani, S2-pani, and Cl2-pani have very strong current response, suggesting increased electrochemical activity and capacity. In contrast, N1-pani, S1-pani, and Cl1-pani have low current response demonstrates its weak reversibility and charge storage capacity. Samples with high ratio of doped graphene outstanding cyclability is due to a composite structure that provides strong electrical conductivity while encouraging a homogeneous SEI that efficiently suppresses continuing negative processes, resulting in high reversibility after the initial creation cycle [87][88].

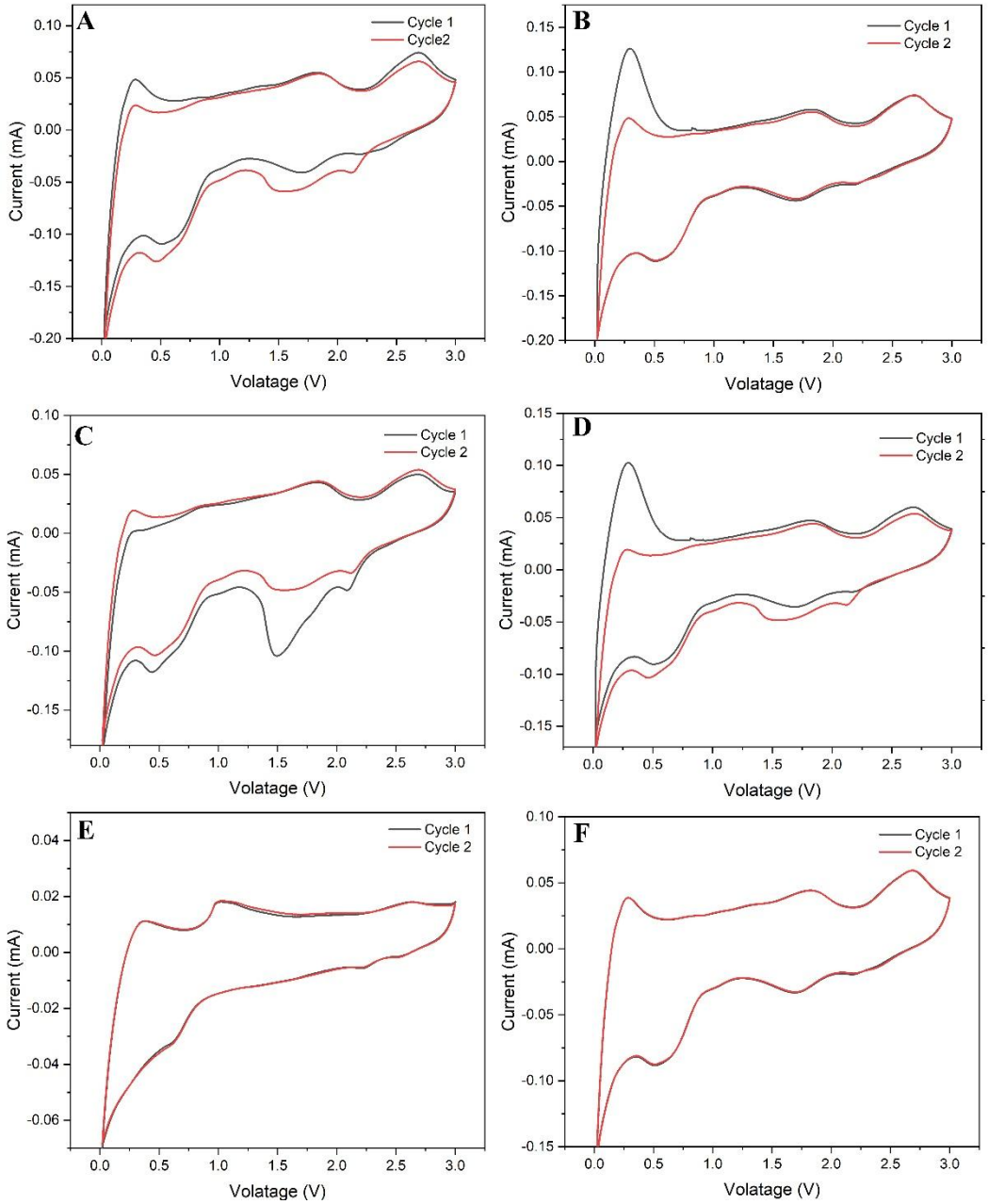


Figure 3.17 Cycling voltammetry of samples, (A) N1-pani, (B) N2- pani, (C) S1-pani, (D) S2- pani, (E) Cl1- pani, and (F) Cl2- pani.

Figure 3.18 A–F present the galvanostatic charge–discharge profiles of N-, S-, and Cl-doped graphene oxide/polyaniline/fumed silica composites evaluated at various current rates from 0.1C to 10C. For all dopant systems, the composites with a high doped graphene oxide content and a low polyaniline ratio (Figure 3.18 B, D, and F) exhibit high specific capacities at low current density and maintain good capacity retention at elevated C-rates, indicating that the continuous polyaniline

network provides efficient electronic pathways and significant pseudocapacitive lithium storage even under fast charge–discharge conditions. The favorable rate performance of these polymer-rich composites arises from the synergistic interaction between polyaniline and doped graphene oxide, where surface-controlled redox reactions in polyaniline enhance charge-transfer kinetics while the graphene framework supports electron transport. In contrast, the reference sample composed of doped graphene oxide and fumed silica without polyaniline exhibits markedly lower capacities and poor rate performance, particularly at high current densities, highlighting the limited lithium storage capability and insufficient charge-transfer kinetics of the polymer-free composite. Although the composites with a lower doped graphene oxide content (N1-pani, S1-pani, and Cl1-pani) (Figure 3.18 A, C, and E) show lower initial capacities at 0.1C compared to the N2-pani, S2-pani, and Cl2-pani samples. Among the dopants studied, the N-doped graphene oxide composites demonstrate the highest reversible capacities and the most stable charge–discharge behavior across all current rates, reflecting the beneficial role of nitrogen-induced electronic modulation and strong lithium-ion adsorption, whereas the S-doped composites show moderate performance with increased polarization and the Cl-doped samples exhibit comparatively lower capacities. Overall, these results clearly demonstrate that polyaniline plays a critical role in enhancing both capacity and high-rate performance, and that an optimized balance between doped graphene oxide, polyaniline, and fumed silica is essential for achieving high-performance lithium-ion battery anodes as shown in Figure 3.19. The inclusion of a moderate amount of polyaniline plays a dual role acting both as a redox-active material and as a soft conducting polymer that bridges structural and electrochemical functions. As a conducting polymer, PANI contributes significantly to enhancing electronic connectivity across the electrode by forming continuous charge transport paths between isolated graphene domains, thereby minimizing internal resistance [89]. Its delocalized π-conjugated backbone enables electron mobility, while its redox-active nature introduces additional pseudocapacitive charge storage through fast, reversible transitions between its leucoemeraldine, emeraldine, and pernigraniline states [90][91][92]. When well-dispersed, as in samples of low ratio of polyaniline, PANI forms a conformal layer over NGO, maximizing interfacial contact and ensuring rapid faradaic reactions at the electrode–electrolyte boundary. Furthermore, PANI's inherent mechanical

flexibility accommodates volume changes during charge–discharge cycles, helping to suppress electrode pulverization and ensuring excellent cycling reversibility. In contrast, the samples with high ratio of polyaniline showed less performance which suffers from overloading of the polymer matrix. PANI forms thicker, less conductive layers, creating electron transport bottlenecks. Excess PANI may block Li^+ diffusion channels and suffer from swelling/shrinking, leading to mechanical instability and structural breakdown during prolonged cycling. Also, the higher PANI content does decrease theoretical capacity of composite since the capacity of polyaniline is less than doped graphene oxide [93]. The excess polymer also results in limited ionic diffusion and poor structural stability due to swelling/shrinking during redox cycling, leading to phase separation and eventual breakdown of the electrode microstructure [89][94].

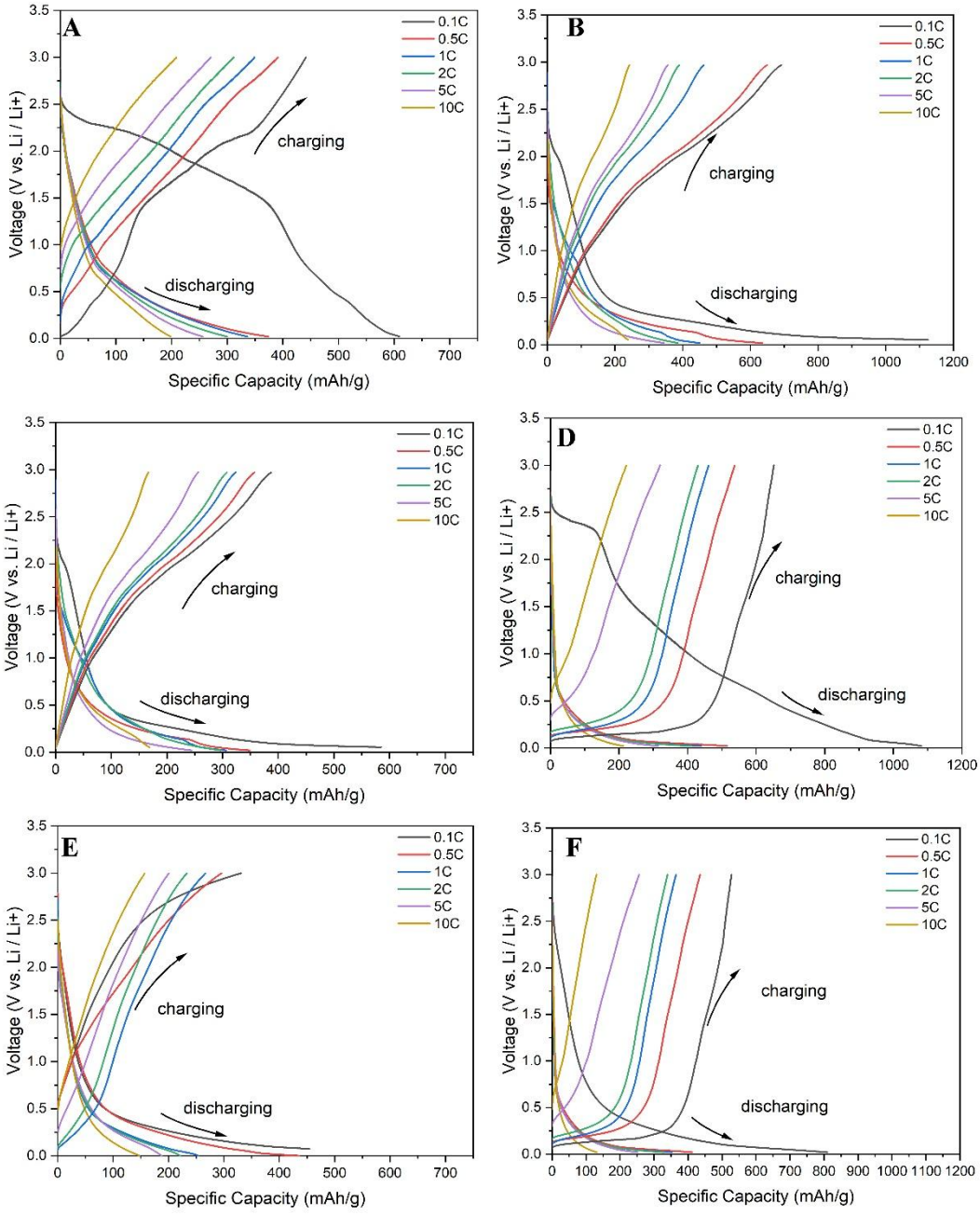


Figure 3.18 Charge-discgarge of samples, (A) N1-pani, (B) N2- pani, (C) S1-pani, (D) S2- pani, (E) Cl1- pani, and (F) Cl2- pani.

Figure 3.20 shows the cycling stability and coulombic efficiency of the N-, S-, and Cl-doped graphene oxide/polyaniline/fumed silica composites over 100 charge–discharge cycles at a high current rate of 10C. This figure shows the samples with high content of doped graphene oxide (N2pani, S2pani, and Cl2pani) show the highest capacity comperd with low content of doped graphene oxide. The N-doped composites (N1 and N2) exhibit the highest reversible capacities and the most stable cycling behavior, retaining capacities of approximately 210–220 mAh g^{-1} after 100

cycles, which indicates excellent structural stability and fast charge-transfer kinetics under high-rate conditions. This superior performance is attributed to nitrogen doping, which enhances electronic conductivity and provides abundant defect sites for lithium-ion adsorption, while the presence of polyaniline contributes additional pseudocapacitive storage and maintains an efficient conductive network during repeated cycling. The S-doped composites (S1 and S2) show moderate cycling stability with slightly lower capacities, suggesting that sulfur-induced defects can enhance lithium storage but also introduce increased polarization and partial structural degradation during long-term high-rate cycling. In contrast, the Cl-doped composites (Cl1 and Cl2) deliver comparatively lower capacities and faster capacity fading, reflecting the weaker interaction between chlorine dopants and lithium ions and less effective electronic structure modulation. Importantly, all polyaniline-containing composites exhibit high and stable coulombic efficiencies approaching ~98–100% after the initial cycles, indicating highly reversible lithium insertion/extraction processes and minimal side reactions at the electrode–electrolyte interface. By comparison, reference samples composed of doped graphene oxide and fumed silica without polyaniline display lower cycling stability and reduced capacity retention, particularly at high current density, highlighting the critical role of polyaniline in improving electrode integrity, buffering volume changes, and sustaining fast charge–discharge performance. Overall, these results demonstrate that the synergistic combination of heteroatom-doped graphene oxide and polyaniline is essential for achieving long-term cycling stability and high-rate durability in lithium-ion battery anodes.

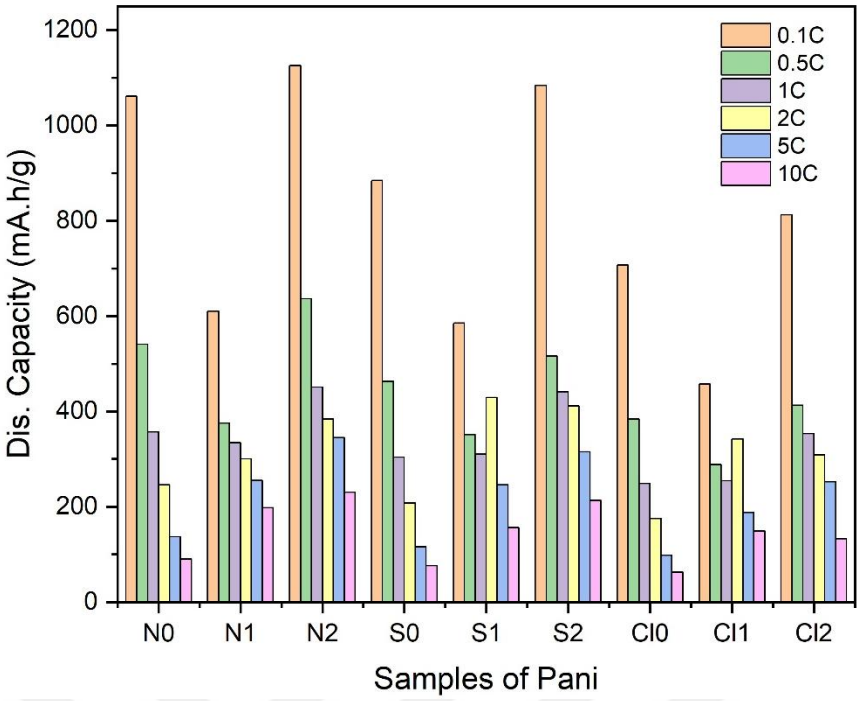


Figure 3.19 Comparasion of discharge capacity for polyaniline samples.

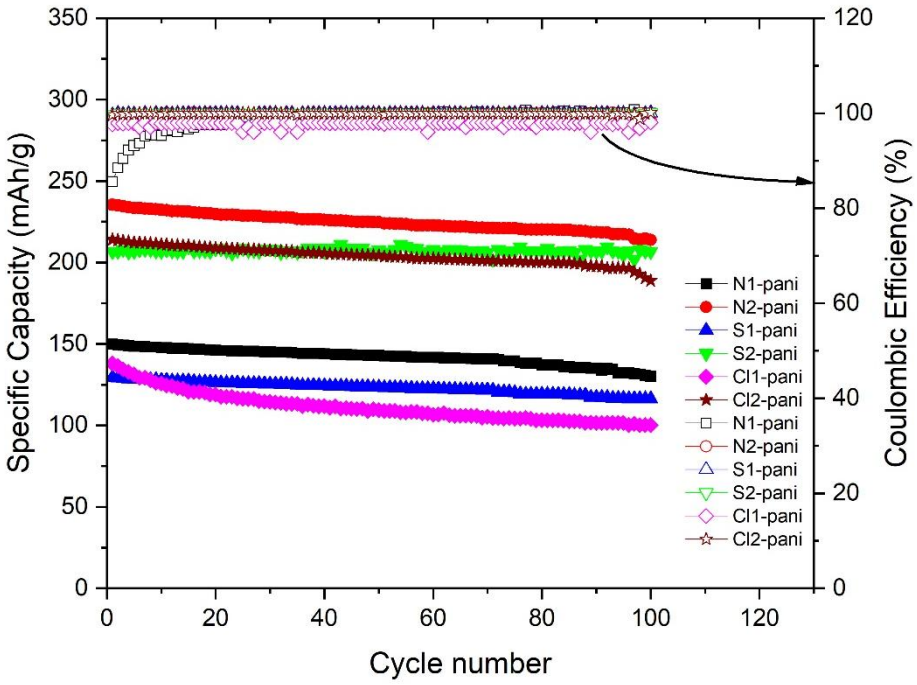


Figure 3.20 Cycling performance of pani samples.

Figure 3.21 A–F present the Nyquist plots of the N-, S-, and Cl-doped graphene oxide/polyaniline/fumed silica composites measured before and after 100 charge–discharge cycles at high current density. All samples exhibit a depressed semicircle in the high-to-medium frequency region followed by an inclined straight line in the low-frequency region, corresponding to the charge-transfer resistance (Rct) at the electrode–electrolyte interface and the Warburg impedance associated with lithium-ion diffusion, respectively. For the N-doped composites (Figure 3.21 A and B), a relatively small semicircle is observed before cycling, indicating low initial Rct, which is attributed to the enhanced electronic conductivity and strong interfacial interaction induced by nitrogen doping. After 100 cycles, only a slight increase in the semicircle diameter is observed, demonstrating excellent interfacial stability and preservation of fast-charge-transfer kinetics, consistent with their superior cycling stability and high-rate performance. The S-doped composites (Figure 3.21 C and D) show a moderate increase in Rct after prolonged cycling, suggesting partial electrode surface reconstruction and increased polarization, which correlates with their moderate capacity retention at high current density. In contrast, the Cl-doped composites (Figure 3.21 E and F) exhibit a pronounced enlargement of the semicircle after 100 cycles, indicating a significant increase in charge-transfer resistance, likely caused by weaker electronic coupling, less effective defect-induced conductivity, and the formation of a thicker or less stable solid electrolyte interphase (SEI). Notably, the inclined low-frequency lines of the polyaniline-containing composites remain relatively steep even after extended cycling, implying sustained lithium-ion diffusion and structural integrity of the electrode framework. These EIS results clearly demonstrate that the synergistic combination of heteroatom-doped graphene oxide and polyaniline effectively reduces interfacial resistance, stabilizes the electrode–electrolyte interface, and supports rapid lithium-ion transport during long-term high-rate cycling, in good agreement with the galvanostatic cycling and rate capability results.

The enhanced performance observed at a low polyaniline ratio further confirms the synergistic effect between N-doped graphene oxide and the conducting polymer, as polyaniline provides fast electron transport pathways and additional pseudocapacitive contribution while buffering volume changes during cycling. Sulfur-doped graphene oxide exhibits moderate electrochemical performance due

to the larger atomic size of sulfur, which expands the interlayer spacing and facilitates Li^+ diffusion; however, its contribution to electronic conductivity and active site density is less pronounced than that of nitrogen, leading to lower overall performance.

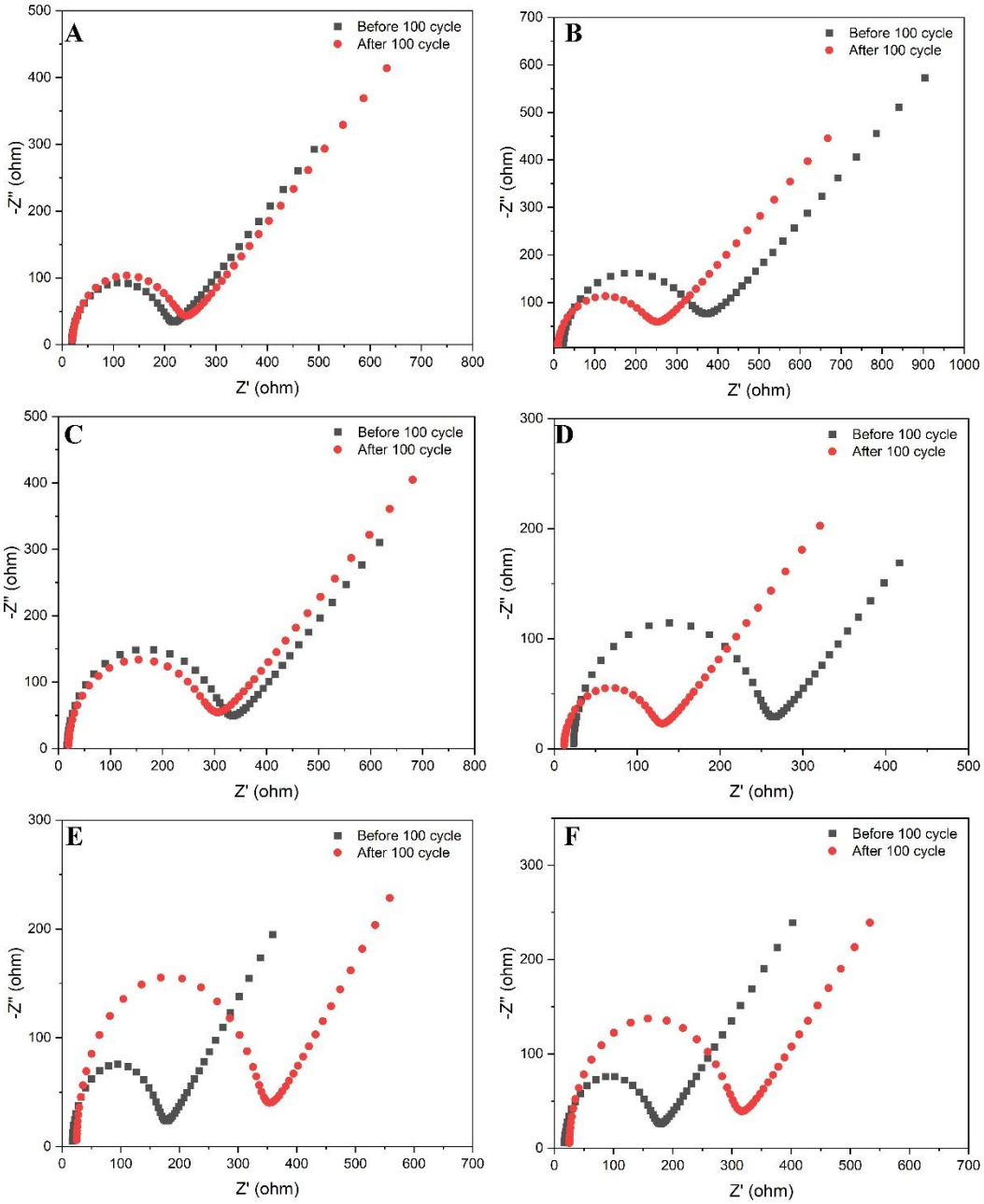


Figure 3.21 EIS of samples, (A) N1-pani, (B) N2- pani, (C) S1- pani, (D) S2- pani, (E) Cl1-pani, and (F) Cl2- pani.

Table 3.7 Resistancs values form EIS before and after cycling of polyaniline samples.

Sample	Rs	Rct	W
N1-pani before cycling	**18,74**	**180,5**	**3.05**
N1- pani 100 cycles	**20,12**	**199,5**	**2.16**
N2- pani before cycling	**22,87**	**310,6**	**1.56**
N2- pani after 100 cycles	**9,725**	**214,2**	**2.00**
S1- pani before cycling	**16,91**	**291,2**	**2.88**
S1- pani after 100 cycles	**19,18**	**258,4**	**2.21**
S2- pani before cycling	**23,18**	**224,9**	**5.29**
S2- pani after 100 cycles	**11,84**	**106,7**	**4.40**
Cl1- pani before cycling	**17,20**	**147,7**	**5**
Cl1- pani after 100 cycles	**24,84**	**306,4**	**3.91**
Cl2- pani before cycling	**16,73**	**148,3**	**3.74**
Cl2-pani after 100 cycles	**25,37**	**269,6**	**3.6**

4
CONCLUSION

In this study, novel composite anode materials consisting of heteroatom-doped graphene oxide (N-GO, S-GO, Cl-GO), conductive polymers (PPy and PANI), and fumed silica were successfully synthesized and systematically evaluated for lithium-ion battery applications. The electrochemical production method enabled the efficient and environmentally friendly synthesis of doped graphene oxide materials under mild conditions. Among the dopants, nitrogen-doped graphene oxide demonstrated the most favorable electrochemical behavior due to enhanced defect density and improved electronic conductivity.

Optimization studies revealed that conductive polymer properties strongly depend on monomer and acid concentration. The PPy sample synthesized with 0.3 M pyrrole and optimized acid concentration exhibited the highest conductivity and suitable surface morphology. Similarly, optimized PANI structures provided improved charge transport pathways. The integration of conductive polymers into the composite structure effectively enhanced electrical conductivity, reduced charge-transfer resistance, and improved electrode integrity. The addition of fumed silica contributed to mechanical stabilization by buffering volume changes during lithiation/delithiation processes. Electrochemical analyses confirmed that composite electrodes outperformed single-component systems in terms of specific capacity, coulombic efficiency, rate capability, and cycling stability.

Electrochemical impedance spectroscopy results indicated reduced charge-transfer resistance and improved lithium-ion diffusion in polymer-supported doped graphene composites. Long-term cycling tests demonstrated that properly engineered composite structures can maintain structural integrity and electrochemical performance even at high current densities (10C).

Overall, the synergistic combination of heteroatom-doped graphene oxide, conductive polymers, and silica provides an effective strategy to overcome the intrinsic limitations of conventional carbon-based anodes. This work offers a promising pathway toward the development of high-capacity, stable, and economically viable anode materials for next-generation lithium-ion batteries, particularly for high-power and long-cycle applications such as electric vehicles and large-scale energy storage systems. Future studies may focus on full-cell configurations, further optimization of composite ratios, and scaling-up processes for industrial applications.

REFERENCES

[1] P. Phogat, “Powering the sustainable future: a review of emerging battery technologies and their environmental,” pp. 3266–3306, 2025, doi: 10.1039/d5su00127g.

[2] N. Nitta, F. Wu, J. T. Lee, and G. Yushin, “Li-ion battery materials: Present and future,” *Mater. Today*, vol. 18, no. 5, pp. 252–264, 2015, doi: 10.1016/j.mattod.2014.10.040.

[3] J. B. Goodenough and K. S. Park, “The Li-ion rechargeable battery: A perspective,” *J. Am. Chem. Soc.*, vol. 135, no. 4, pp. 1167–1176, 2013, doi: 10.1021/ja3091438.

[4] P. Das and B. C. Thompson, “Development of design strategies for conjugated polymer binders in lithium-ion batteries,” pp. 317–341, 2023, doi: 10.1038/s41428-022-00708-x.

[5] P. Poizot, S. Laruelle, S. Grugeon, L. Dupont, and J. Tarascon, “Nano-sized transition-metal oxides as negative-electrode materials for lithium-ion batteries,” vol. 407, no. September, 2000.

[6] J. Cabana, L. Monconduit, D. Larcher, and M. R. Palacín, “Beyond intercalation-based Li-ion batteries: The state of the art and challenges of electrode materials reacting through conversion reactions,” *Adv. Mater.*, vol. 22, no. 35, pp. 170–192, 2010, doi: 10.1002/adma.201000717.

[7] V. H. Nguyen and Y. H. Kim, “Recent advances in cathode and anode materials for lithium ion batteries,” *Appl. Chem. Eng.*, vol. 29, no. 6, pp. 635–644, 2018, doi: 10.14478/ace.2018.1092.

[8] M. N. Obrovac and V. L. Chevrier, “Alloy negative electrodes for Li-ion batteries,” *Chem. Rev.*, vol. 114, no. 23, pp. 11444–11502, 2014, doi: 10.1021/cr500207g.

[9] S. D. Beattie, D. Larcher, M. Morcrette, and B. Simon, “Si Electrodes for Li-Ion Batteries — A New Way to Look at an Old Problem,” pp. 158–163, 2008, doi: 10.1149/1.2817828.

[10] X. Zhou, Y. Liu, C. Du, Y. Ren, T. Mu, and P. Zuo, “Polyaniline-encapsulated silicon on three-dimensional carbon nanotubes foam with enhanced electrochemical performance for lithium-ion batteries,” *J. Power Sources*, vol. 381, no. December 2017, pp. 156–163, 2018, doi: 10.1016/j.jpowsour.2018.02.009.

[11] J. Cai, P. Zuo, X. Cheng, Y. Xu, and G. Yin, “Nano-silicon/polyaniline composite for lithium storage,” *Electrochem. commun.*, vol. 12, no. 11, pp.

1572–1575, 2010, doi: 10.1016/j.elecom.2010.08.036.

[12] M. Kummer *et al.*, “Silicon/Polyaniline Nanocomposites as Anode Material for Lithium Ion Batteries,” *J. Electrochem. Soc.*, vol. 161, no. 1, pp. A40–A45, 2014, doi: 10.1149/2.020401jes.

[13] N. Yan *et al.*, “Hollow Porous SiO2 nanocubes towards high-performance anodes for lithium-ion batteries,” *Sci. Rep.*, vol. 3, pp. 1–6, 2013, doi: 10.1038/srep01568.

[14] M. T. Mcdowell, S. W. Lee, W. D. Nix, and Y. Cui, “25th Anniversary Article : Understanding the Lithiation of Silicon and Other Alloying Anodes for Lithium-Ion Batteries,” pp. 4966–4985, 2013, doi: 10.1002/adma.201301795.

[15] V. A. Sethuraman, J. Electrochem, A. Soc, and M. Chi, “In Situ Measurements of Stress-Potential Coupling in Lithiated Silicon In Situ Measurements of Stress-Potential Coupling in Lithiated,” 2010, doi: 10.1149/1.3489378.

[16] M. Thakur, M. Isaacson, S. L. Sinsabaugh, M. S. Wong, and S. Lisa, “Gold-coated porous silicon films as anodes for lithium ion batteries,” *J. Power Sources*, vol. 205, pp. 426–432, 2012, doi: 10.1016/j.jpowsour.2012.01.058.

[17] Y. Y. Tang *et al.*, “Electrochimica Acta Cobalt nanomountain array supported silicon film anode for high-performance lithium ion batteries,” vol. 88, pp. 664–670, 2013, doi: 10.1016/j.electacta.2012.10.119.

[18] M. Wang, L. Fan, M. Huang, J. Li, and X. Qu, “Conversion of diatomite to porous Si / C composites as promising anode materials for lithium-ion batteries,” *J. Power Sources*, vol. 219, pp. 29–35, 2012, doi: 10.1016/j.jpowsour.2012.06.102.

[19] T. Song *et al.*, “Arrays of Sealed Silicon Nanotubes As Anodes for Lithium Ion Batteries,” pp. 1710–1716, 2010, doi: 10.1021/nl100086e.

[20] X. Zhou, J. Tang, J. Yang, J. Xie, and L. Ma, “Electrochimica Acta Silicon @ carbon hollow core – shell heterostructures novel anode materials for lithium ion batteries,” vol. 87, pp. 663–668, 2013, doi: 10.1016/j.electacta.2012.10.008.

[21] N. Liu, H. Wu, M. T. Mcdowell, Y. Yao, C. Wang, and Y. Cui, “A Yolk-Shell Design for Stabilized and Scalable Li-Ion Battery Alloy Anodes,” 2012.

[22] H. Wu, G. Zheng, N. Liu, T. J. Carney, Y. Yang, and Y. Cui, “Engineering Empty Space between Si Nanoparticles for Lithium-Ion Battery Anodes,” 2012.

[23] Z. P. Guo, J. Electrochem, and A. Soc, “Silicon / Disordered Carbon Nanocomposites for Lithium-Ion Battery Anodes Silicon / Disordered Carbon Nanocomposites for Lithium-Ion,” 2005, doi: 10.1149/1.2051847.

[24] Y. Zhang *et al.*, “Composite anode material of silicon / graphite / carbon nanotubes for Li-ion batteries,” vol. c, pp. 4994–5000, 2006, doi: 10.1016/j.electacta.2006.01.043.

[25] L. Shen, X. Guo, X. Fang, Z. Wang, and L. Chen, “Magnesiothermically

reduced diatomaceous earth as a porous silicon anode material for lithium ion batteries," *J. Power Sources*, vol. 213, pp. 229–232, 2012, doi: 10.1016/j.jpowsour.2012.03.097.

[26] H. Xiang *et al.*, "Graphene / nanosized silicon composites for lithium battery anodes with improved cycling stability," vol. c, pp. 0–9, 2011, doi: 10.1016/j.carbon.2011.01.002.

[27] X. Zhou, Y. Yin, L. Wan, and Y. Guo, "Facile synthesis of silicon nanoparticles inserted into graphene sheets as improved anode materials for lithium-ion batteries w," *ChemComm*, pp. 2198–2200, 2012, doi: 10.1039/c2cc17061b.

[28] X. Xiao *et al.*, "Phase-separated silicon e tin nanocomposites for high capacity negative electrodes in lithium ion batteries," *J. Power Sources*, vol. 214, pp. 258–265, 2012, doi: 10.1016/j.jpowsour.2012.04.028.

[29] J. M. Yan, H. Z. Huang, J. Zhang, and Y. Yang, "The study of Mg2Si / carbon composites as anode materials for lithium ion batteries," vol. c, pp. 547–552, 2008, doi: 10.1016/j.jpowsour.2007.06.074.

[30] U. Kasavajjula, C. Wang, and A. J. Appleby, "Nano- and bulk-silicon-based insertion anodes for lithium-ion secondary cells," vol. 163, pp. 1003–1039, 2007, doi: 10.1016/j.jpowsour.2006.09.084.

[31] J. Lee *et al.*, "Improvement of electrochemical behavior of Sn 2 Fe / C nanocomposite anode with Al 2 O 3 addition for lithium-ion batteries," *J. Power Sources*, vol. 195, no. 15, pp. 5044–5048, 2010, doi: 10.1016/j.jpowsour.2010.02.068.

[32] Y. Liu *et al.*, "Improvement of cycling stability of Si anode by mechanochemcial reduction and carbon coating," vol. 189, pp. 480–484, 2009, doi: 10.1016/j.jpowsour.2008.12.045.

[33] X. N. Zhang, G. L. Pan, G. R. Li, J. Q. Qu, and X. P. Gao, "Si – Si3N4 composites as anode materials for lithium ion batteries," vol. v, pp. 1107–1112, 2007, doi: 10.1016/j.ssi.2007.05.011.

[34] G. X. Wang, L. Sun, D. H. Bradhurst, S. Zhong, S. X. Dou, and H. K. Liu, "Nanocrystalline NiSi alloy as an anode material for lithium-ion batteries," vol. 306, pp. 249–252, 2000.

[35] H. Lee and S. Lee, "Carbon-coated nano-Si dispersed oxides / graphite composites as anode material for lithium ion batteries," vol. 6, pp. 465–469, 2004, doi: 10.1016/j.elecom.2004.03.005.

[36] J. M. Chem, "Nano-silicon composites using poly(3,4-ethylenedioxythiophene):poly (styrenesulfonate) as elastic polymer matrix and carbon source for lithium-ion battery anode," *J. Mater. Chem.*, pp. 1094–1099, 2012, doi: 10.1039/c1jm14568a.

[37] S. Y. Chew, S. H. Ng, L. Zhao, and H. K. Liu, "Novel nano-silicon / polypyrrole composites for lithium storage," vol. c, pp. 941–946, 2007, doi: 10.1016/j.elecom.2006.11.028.

[38] F. Article, "Silicon nanowires for Li-based battery anodes : a review," 2013, doi: 10.1039/c3ta11714f.

[39] H. Chen, Y. Xiao, L. Wang, and Y. Yang, “Silicon nanowires coated with copper layer as anode materials for lithium-ion batteries,” *J. Power Sources*, vol. 196, no. 16, pp. 6657–6662, 2011, doi: 10.1016/j.jpowsour.2010.12.075.

[40] J. Qu *et al.*, “Self-aligned Cu – Si core – shell nanowire array as a high-performance anode for Li-ion batteries,” *J. Power Sources*, vol. 198, pp. 312–317, 2012, doi: 10.1016/j.jpowsour.2011.10.004.

[41] W. Chen *et al.*, “Facile synthesis of silicon fi lms by photosintering as anode materials for lithium-ion batteries,” *J. Power Sources*, vol. 214, pp. 21–27, 2012, doi: 10.1016/j.jpowsour.2012.04.047.

[42] B. Peng *et al.*, “Lithium transport at silicon thin film : Barrier for high-rate capability anode Lithium transport at silicon thin film : Barrier for high-rate capability anode,” vol. 034701, 2010, doi: 10.1063/1.3462998.

[43] M. G. Ersozoglu, H. Gursu, M. Gencten, A. S. Sarac, and Y. Sahin, “A green approach to fabricate binder-free S-doped graphene oxide electrodes for vanadium redox battery,” *Int. J. Energy Res.*, vol. 45, no. 2, pp. 2126–2137, 2021, doi: 10.1002/er.5906.

[44] M. B. Arvas, H. Gürsu, M. Gencten, and Y. Sahin, “New Approach Synthesis of S, N Co-Doped Graphenes for High-Performance Supercapacitors,” *ChemistrySelect*, vol. 7, no. 21, 2022, doi: 10.1002/slct.202200360.

[45] H. Gürsu, M. Gençten, and Y. Şahin, “One-step electrochemical preparation of graphene-coated pencil graphite electrodes by cyclic voltammetry and their application in vanadium redox batteries,” *Electrochim. Acta*, vol. 243, pp. 239–249, 2017, doi: 10.1016/j.electacta.2017.05.065.

[46] S. Stankovich *et al.*, “Synthesis of graphene-based nanosheets via chemical reduction of exfoliated graphite oxide,” *Carbon N. Y.*, vol. 45, no. 7, pp. 1558–1565, 2007, doi: 10.1016/j.carbon.2007.02.034.

[47] G. Kalita, M. Masahiro, H. Uchida, K. Wakita, and M. Umeno, “Few layers of graphene as transparent electrode from botanical derivative camphor,” *Mater. Lett.*, vol. 64, no. 20, pp. 2180–2183, 2010, doi: 10.1016/j.matlet.2010.07.005.

[48] R. Joy *et al.*, “Graphene: Chemistry and Applications for Lithium-Ion Batteries,” *Electrochem*, vol. 3, no. 1, pp. 143–183, 2022, doi: 10.3390/electrochem3010010.

[49] S. Yasa, O. Kumbasi, M. B. Arvas, M. Gencten, M. Sahin, and Y. Sahin, “S-Doped Graphene Oxide/N-Doped Graphene Oxide/PANI: A Triple Composite for High-Performance Supercapacitor Applications,” *ECS J. Solid State Sci. Technol.*, vol. 12, no. 5, p. 051002, May 2023, doi: 10.1149/2162-8777/acd3af.

[50] A. Mansuroglu, M. Gencten, M. B. Arvas, M. Sahin, and Y. Sahin, “Investigation the effects of chlorine doped graphene oxide as an electrolyte additive for gel type valve regulated lead acid batteries,” *J. Energy Storage*, vol. 64, no. July 2022, p. 107224, Aug. 2023.

[51] P. Sengodu and A. D. Deshmukh, “Conducting polymers and their inorganic composites for advanced Li-ion batteries: A review,” *RSC Adv.*, vol. 5, no. 52, pp. 42109–42130, 2015, doi: 10.1039/c4ra17254j.

[52] A. Manickavasagan, R. Ramachandran, S. M. Chen, and M. Velluchamy, “Ultrasonic assisted fabrication of silver tungstate encrusted polypyrrole nanocomposite for effective photocatalytic and electrocatalytic applications,” *Ultrason. Sonochem.*, vol. 64, no. September 2019, p. 104913, 2020, doi: 10.1016/j.ultsonch.2019.104913.

[53] Z. Jiao, Y. Zhang, and H. Fan, “Ultrasonic-microwave method in preparation of polypyrrole-coated magnetic particles for vitamin D extraction in milk,” *J. Chromatogr. A*, vol. 1457, pp. 7–13, 2016, doi: 10.1016/j.chroma.2016.06.041.

[54] S. Majumdar, K. Sarmah, and D. Mahanta, “A Simple Route to Prepare Polypyrrole-Coated Filter Papers via Vapor Phase Polymerization and Their Gas Sensing Application,” *ACS Appl. Polym. Mater.*, vol. 2, no. 5, pp. 1933–1942, 2020, doi: 10.1021/acsapm.0c00147.

[55] Z. Hanif, D. Shin, D. Choi, and S. J. Park, “Development of a vapor phase polymerization method using a wet-on-wet process to coat polypyrrole on never-dried nanocellulose crystals for fabrication of compression strain sensor,” *Chem. Eng. J.*, vol. 381, no. September 2019, p. 122700, 2020, doi: 10.1016/j.cej.2019.122700.

[56] J. Li, Y. He, Y. Sun, X. Zhang, W. Shi, and D. Ge, “Synthesis of polypyrrole/V2O5 composite film on the surface of magnesium using a mild vapor phase polymerization (VPP) method for corrosion resistance,” *Coatings*, vol. 10, no. 4, 2020, doi: 10.3390/coatings10040402.

[57] M. Šetka, R. Calavia, L. Vojkůvka, E. Llobet, J. Drbohlavová, and S. Vallejos, “Raman and XPS studies of ammonia sensitive polypyrrole nanorods and nanoparticles,” *Sci. Rep.*, vol. 9, no. 1, pp. 1–10, 2019, doi: 10.1038/s41598-019-44900-1.

[58] D. Dosenovicova *et al.*, “Selective photoelectrochemical deposition of polypyrrole onto hydrogenated a-Si for optoelectronic applications,” *Mater. Sci. Semicond. Process.*, vol. 68, no. May, pp. 1–5, 2017, doi: 10.1016/j.mssp.2017.05.028.

[59] Y. Cong, S. Liu, and H. Chen, “Fabrication of conductive polypyrrole nanofibers by electrospinning,” *J. Nanomater.*, vol. 2013, pp. 1–7, 2013, doi: 10.1155/2013/148347.

[60] F. Khadem, M. Pishvaei, M. Salami-Kalajahi, and F. Najafi, “Morphology control of conducting polypyrrole nanostructures via operational conditions in the emulsion polymerization,” *J. Appl. Polym. Sci.*, vol. 134, no. 15, pp. 1–7, 2017, doi: 10.1002/app.44697.

[61] S. Krishnaswamy, V. Ragupathi, S. Raman, P. Panigrahi, and G. S. Nagarajan, “Optical properties of P- type polypyrrole thin film synthesized by pulse laser deposition technique: Hole transport layer in electroluminescence devices,” *Optik (Stuttg).*, vol. 194, no. February, p. 163034, 2019, doi: 10.1016/j.ijleo.2019.163034.

[62] A. Mahun, S. Abbrent, P. Bober, J. Brus, and L. Kobera, “Effect of structural features of polypyrrole (PPy) on electrical conductivity reflected on 13C ssNMR parameters,” *Synth. Met.*, vol. 259, no. December 2019, pp. 3–8, 2020, doi: 10.1016/j.synthmet.2019.116250.

[63] S. Zhang, G. Lv, G. Wang, K. Zhu, D. Yu, and J. Shao, “Effects of UV radiation on the preparation of polypyrrole in the presence of hydrogen peroxide,” *Radiat. Eff. Defects Solids*, vol. 170, no. 10, pp. 821–831, 2015, doi: 10.1080/10420150.2015.1116071.

[64] K. Namsheer and C. S. Rout, “Conducting polymers: a comprehensive review on recent advances in synthesis, properties and applications,” *RSC Adv.*, vol. 11, no. 10, pp. 5659–5697, 2021, doi: 10.1039/d0ra07800j.

[65] T. Uyar, L. Toppare, and J. Hacaloğlu, “Spectroscopic investigation of oxidation of p-toluene sulfonic acid doped polypyrrole,” *Synth. Met.*, vol. 123, no. 2, pp. 335–342, 2001, doi: 10.1016/S0379-6779(01)00311-3.

[66] A. Yussuf, M. Al-Saleh, S. Al-Enezi, and G. Abraham, “Synthesis and Characterization of Conductive Polypyrrole: The Influence of the Oxidants and Monomer on the Electrical, Thermal, and Morphological Properties,” *Int. J. Polym. Sci.*, vol. 2018, 2018, doi: 10.1155/2018/4191747.

[67] S. Nosheen *et al.*, “Synthesis and Characterization of Polypyrrole Synthesized via Different Routes,” vol. 9, no. 06, pp. 1630–1633, 2020.

[68] J. Stejskal, I. Sapurina, and M. Trchová, “Polyaniline nanostructures and the role of aniline oligomers in their formation,” *Prog. Polym. Sci.*, vol. 35, no. 12, pp. 1420–1481, 2010, doi: 10.1016/j.progpolymsci.2010.07.006.

[69] S. Bhadra, D. Khastgir, N. K. Singha, and J. H. Lee, “Progress in preparation, processing and applications of polyaniline,” *Prog. Polym. Sci.*, vol. 34, no. 8, pp. 783–810, 2009, doi: 10.1016/j.progpolymsci.2009.04.003.

[70] N. Gospodinova and L. Terlemezyan, “Conducting polymers prepared by oxidative polymerization: Polyaniline,” *Prog. Polym. Sci.*, vol. 23, no. 8, pp. 1443–1484, 1998, doi: 10.1016/S0079-6700(98)00008-2.

[71] L. Zhang, Z. D. Zujovic, H. Peng, G. A. Bowmaker, P. A. Kilmartin, and J. Travas-Sejdic, “Structural characteristics of polyaniline nanotubes synthesized from different buffer solutions,” *Macromolecules*, vol. 41, no. 22, pp. 8877–8884, 2008, doi: 10.1021/ma801728j.

[72] Y. Shi and G. Yu, “Designing Hierarchically Nanostructured Conductive Polymer Gels for Electrochemical Energy Storage and Conversion,” *Chem. Mater.*, vol. 28, no. 8, pp. 2466–2477, 2016, doi: 10.1021/acs.chemmater.5b04879.

[73] C. Wang, Z. Guo, R. Hong, J. Gao, Y. Guo, and C. Gu, “A novel method for synthesis of polyaniline and its application for catalytic degradation of atrazine in a Fenton-like system,” *Chemosphere*, vol. 197, pp. 576–584, 2018, doi: 10.1016/j.chemosphere.2018.01.050.

[74] K. Y. Lin *et al.*, “Characterization of polyaniline synthesized from chemical oxidative polymerization at various polymerization temperatures,” *Eur. Polym. J.*, vol. 88, pp. 311–319, 2017, doi: 10.1016/j.eurpolymj.2017.01.035.

[75] H. Gürsu *et al.*, “Preparation of N-doped graphene powders by cyclic voltammetry and a potential application of them: Anode materials of Li-ion batteries,” *Int. J. Energy Res.*, vol. 43, no. 10, pp. 5346–5354, Aug. 2019, doi: 10.1002/er.4618.

[76] H. Gürsu *et al.*, "A novel green and one-step electrochemical method for production of sulfur-doped graphene powders and their performance as an anode in Li-ion battery," *Ionics (Kiel).*, vol. 26, no. 10, pp. 4909–4919, 2020, doi: 10.1007/s11581-020-03671-w.

[77] H. Gursu *et al.*, "Production of chlorine-containing functional group doped graphene powders using Yucel's method as anode materials for Li-ion batteries," *RSC Adv.*, vol. 11, no. 63, pp. 40059–40071, 2021, doi: 10.1039/d1ra07653a.

[78] Z. Xing *et al.*, "One-pot hydrothermal synthesis of Nitrogen-doped graphene as high-performance anode materials for lithium ion batteries," *Sci. Rep.*, vol. 6, no. November 2015, pp. 1–10, 2016, doi: 10.1038/srep26146.

[79] M. B. Arvas, N. Karatepe, M. Gencten, and Y. Sahin, "Fabrication of high-performance symmetrical coin cell supercapacitors by using one step and green synthesis sulfur doped graphene powders," *New J. Chem.*, vol. 45, no. 15, pp. 6928–6939, 2021, doi: 10.1039/d0nj06061e.

[80] L. Shi *et al.*, "SiOx microparticles embedded into 3D wrinkled N, S co-doped multilayer graphene sheets as a high-performance anode for long-life full lithium-ion batteries," *Electrochim. Acta*, vol. 390, p. 138841, 2021, doi: 10.1016/j.electacta.2021.138841.

[81] R. Yu, R. Jiang, and Z. Zhou, "Graphene, a one-atom-thick carbon sheet, has been proposed for use in combination with SiO2 materials due to its unique features, including high electron mobility, electrochemical stability, enormous surface area, and mechanical strength, which have gener," *J. Alloys Compd.*, vol. 937, p. 168324, 2023, doi: 10.1016/j.jallcom.2022.168324.

[82] S. Gao *et al.*, "Twin-Graphene : A Promising Anode Material for Lithium-Ion Batteries with Ultrahigh Specific Capacity," 2023, doi: 10.1021/acs.jpcc.3c01872.

[83] J. Chen, M. W. Xu, J. Wu, and C. M. Li, "Center-iodized graphene as an advanced anode material to significantly boost the performance of lithium-ion batteries," *Nanoscale*, vol. 10, no. 19, pp. 9115–9122, 2018, doi: 10.1039/c8nr00061a.

[84] G. X. Wang, L. Yang, Y. Chen, J. Z. Wang, S. Bewlay, and H. K. Liu, "An investigation of polypyrrole-LiFePO4 composite cathode materials for lithium-ion batteries," *Electrochim. Acta*, vol. 50, no. 24, pp. 4649–4654, 2005, doi: 10.1016/j.electacta.2005.02.026.

[85] Q. Wei *et al.*, "Novel honeycomb silicon wrapped in reduced graphene oxide/CNT system as high-stability anodes for lithium-ion batteries," *Electrochim. Acta*, vol. 317, pp. 583–593, 2019, doi: 10.1016/j.electacta.2019.06.024.

[86] Z. Favors, W. Wang, H. H. Bay, A. George, M. Ozkan, and C. S. Ozkan, "Stable cycling of SiO2 nanotubes as high-performance anodes for lithium-ion batteries," *Sci. Rep.*, vol. 4, pp. 1–7, 2014, doi: 10.1038/srep04605.

[87] Z. Wang *et al.*, "Aluminum as a bi-functional reducing agent for the fabrication of graphene encapsulated silicon microspheres as anodes for

high-performance lithium-ion batteries," *J. Alloys Compd.*, vol. 936, p. 168205, 2023, doi: 10.1016/j.jallcom.2022.168205.

[88] C. Shan *et al.*, "Graphene Oxides Used as a New 'dual Role' Binder for Stabilizing Silicon Nanoparticles in Lithium-Ion Battery," *ACS Appl. Mater. Interfaces*, vol. 10, no. 18, pp. 15665–15672, 2018, doi: 10.1021/acsami.8b00649.

[89] G. A. Snook, P. Kao, and A. S. Best, "Conducting-polymer-based supercapacitor devices and electrodes," *J. Power Sources*, vol. 196, no. 1, pp. 1–12, 2011, doi: 10.1016/j.jpowsour.2010.06.084.

[90] K. Zhang, L. L. Zhang, X. S. Zhao, and J. Wu, "Graphene/polyaniline nanofiber composites as supercapacitor electrodes," *Chem. Mater.*, vol. 22, no. 4, pp. 1392–1401, 2010, doi: 10.1021/cm902876u.

[91] Y. Chen, "A review of polyaniline based materials as anodes for lithiumion batteries," *IOP Conf. Ser. Mater. Sci. Eng.*, vol. 677, no. 2, 2019, doi: 10.1088/1757-899X/677/2/022115.

[92] Y. Luo *et al.*, "Application of Polyaniline for Li-Ion Batteries, Lithium–Sulfur Batteries, and Supercapacitors," *ChemSusChem*, vol. 12, no. 8, pp. 1591–1611, 2019, doi: 10.1002/cssc.201802186.

[93] R. Zhao, Z. Chang, X. Fu, M. Xu, X. Ai, and J. Qian, "Revisit of Polyaniline as a High-Capacity Organic Cathode Material for Li-Ion Batteries," *Polymers (Basel).*, vol. 16, no. 10, pp. 1–9, 2024, doi: 10.3390/polym16101401.

[94] W. Tan, J. C. Stallard, C. Jo, M. F. L. De Volder, and N. A. Fleck, "The mechanical and electrochemical properties of polyaniline-coated carbon nanotube mat," *J. Energy Storage*, vol. 41, no. April, p. 102757, 2021, doi: 10.1016/j.est.2021.102757.

PUBLICATIONS FROM THE THESIS

Conference Papers

1. A Tripartite Composite Incorporating Chlorine-Doped Graphene Oxide, polyaniline, and Silica for Lithium-Ion Battery Anodes

Papers

1. M. Al-Bujasim, M. GENÇTEN, K. B. Dönmez, M. B. Arvas, N. Karatepe, and Y. Sahin, "A Tripartite Composite Incorporating Nitrogen-Doped Graphene Oxide, Polypyrrole, and Silica for Lithium-Ion Battery Anodes," ECS J. Solid State Sci. Technol., Apr. 2024, doi: 10.1149/2162-8777/ad423b.

2. M. Al-Bujasim, M. Gencten, K. B. Donmez, M. B. Arvas, N. Karatepe, and Y. Sahin, "Enhanced lithium-ion battery performance with a novel composite anode: S-doped graphene oxide, polypyrrole, and fumed silica," Nanotechnology, vol. 36, no. 11, 2025, doi: 10.1088/1361-6528/ada039.

3. M. Al-Bujasim and M. Gencten, "Synergistic Integration of Nitrogen-Doped Graphene Oxide, Silica, and Polyaniline for High-Performance Lithium-Ion Battery Anodes," J. Electrochem. Soc., vol. 172, no. 12, p. 120514, 2025, doi: 10.1149/1945-7111/ae283d.

Projects

1. Yarım hücre ve tam hücre Li-ion Piller için Kompozit Formda Yeni Nesil Anot Malzemelerinin Üretimi ve Performans Araştırması.

2. Polipirol/Heteroatom Katkılı Grafen Oksit/Silisyum Oksit Esaslı Kompozit Malzemelerin Üretimi ve Li-iyon Pillerde Anot Malzemesi Olarak Kullanımlarının Araştırılması

3. Li-iyon Bataryalar İçin Kompozit Formda Yeni Nesil Anot Malzemelerinin Üretimi Ve Performanslarının İncelenmesi.